International Journal of Mechanical Sciences 317 (2026) 111499

Contents lists available at ScienceDirect

International Journal of Mechanical Sciences

journal homepage: www.elsevier.com/locate/ijmecsci

Virtual local resonance enabled by chirality-removed defects in chiral metamaterials

Yupei Jian [a,*], Cuipeng Xia [b,*], Weiqun Liu [c], Yao Wu [b], Guobiao Hu [d]

[a] School of Electrical Engineering, Southwest Jiaotong University, Chengdu, Sichuan 610031, China
[b] Department of Mechanical and Mechatronics Engineering, The University of Auckland, Auckland 1010, New Zealand
[c] School of Mechanical Engineering, Southwest Jiaotong University, Chengdu, Sichuan 610031, China
[d] Internet of Things Thrust, The Hong Kong University of Science and Technology (Guangzhou), Guangzhou, Guangdong 511400, China

ARTICLE INFO

Keywords:
Chiral metamaterials
Broadband vibration suppression
Band gap mechanism
Defect
Mode transition, Virtual local resonance

ABSTRACT

Although local resonance mechanisms are effective for subwavelength wave control, their use in broadband low-frequency vibration attenuation is fundamentally constrained by the mass-stiffness trade-off. In this study, we report a novel virtual locally resonant (VLR) band gap that overcomes this limitation by producing resonant behavior through mode transitions rather than by discrete physical resonators. Firstly, using a lumped-parameter model and finite element analysis, we show that the chirality variations between isotactic and syndiotactic lattices with compression-torsion coupling induce mode transitions that strongly influence band gap formation. Inspired by this insight, chirality-removed defects are introduced into an isotactic lattice. The resulting impedance mismatch at periodic interfaces forces longitudinal waves to convert into pure torsional resonances localized at the defects, yielding a band gap that exhibits the antiresonance peak and subwavelength characteristics of conventional locally resonant (LR) gaps. Crucially, since the resonance emerges virtually from mode transition, the proposed mechanism eliminates the need for heavy physical resonators. A systematic parametric study demonstrates flexible tunability of the VLR band gap via rotational inertia and torsional stiffness, and further shows that graded designs enable the overlap of discrete gaps to achieve ultra-broadband attenuation. Finally, the numerical predictions were validated experimentally, and a lightweight graded prototype achieved an ultra-wide low-frequency suppression band spanning 170.6–1933.6 Hz. This VLR mechanism offers a new pathway to lightweight, high-stiffness metamaterials for broad low-frequency vibration suppression.

1. Introduction

Mechanical vibrations are pervasive in engineering systems such as civil infrastructure, transportation equipment, and industrial environments, where they can critically affect structural safety, ride comfort, and operational precision [1–4]. Recently, artificially designed metamaterials with unconventional mechanical and physical properties have emerged as an effective approach for vibration mitigation. Their band gap suppresses wave propagation while maintaining load-bearing capacity [5], which makes them highly attractive for vibration and noise attenuation [6–9], filtering [10–12], and wave-guiding applications [13–15].

Two classical band-gap formation mechanisms, i.e., Bragg scattering (BS) and local resonance (LR), have been established for elastic and acoustic wave manipulation. BS band gaps result from periodic impedance mismatches that produce destructive interference, enabling simple designs and broadband attenuation [16,17]. However, the attenuation strength is limited, and achieving subwavelength control typically requires large lattice constants or low-modulus materials, which impose space and stability constraints [18,19]. To address these limitations, designs such as truss-based lattices [20,21] and lattice sandwich structures [22–24] have been proposed to reduce lattice size while improving the strength-to-weight ratio. In contrast, LR band gaps arise from out-of-phase motion between resonators and the host structure, enabling strong low-frequency attenuation in compact lattices without compromising static stiffness [25–27]. However, these band gaps are commonly narrow, and bandwidth enlargement often relies on increasing resonator mass or the volume filling fraction, which raises system mass and complicates fabrication at small scales [28,29]. Accordingly, strategies including multi-degree-of-freedom resonators

* Corresponding authors.
E-mail addresses: yupeijian@swjtu.edu.cn (Y. Jian), cxia144@aucklanduni.ac.nz (C. Xia).

https://doi.org/10.1016/j.ijmecsci.2026.111499
Received 21 January 2026; Received in revised form 3 March 2026; Accepted 9 March 2026
Available online 10 March 2026

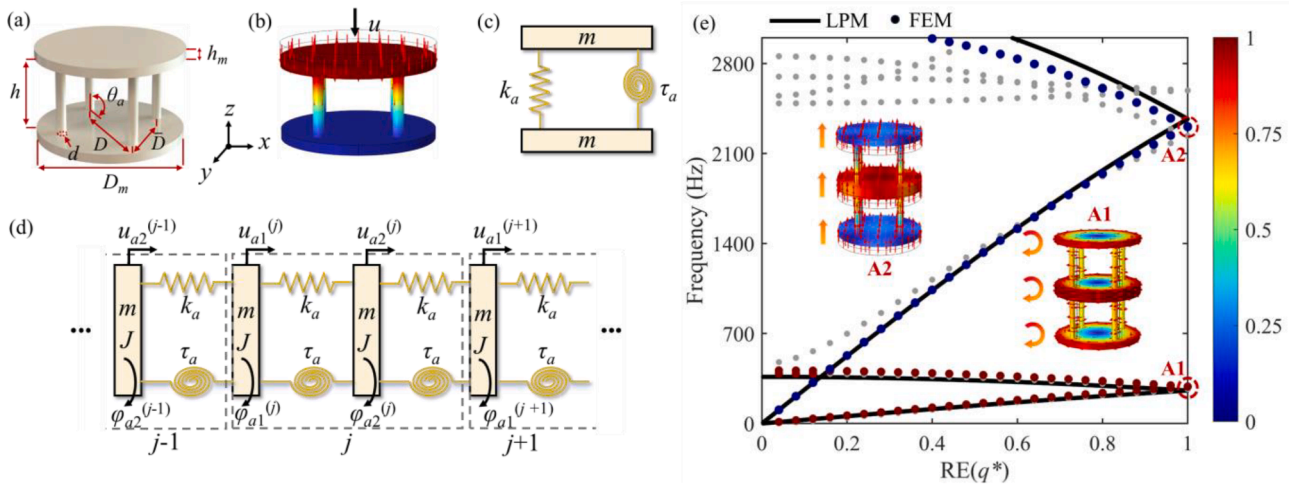

Fig. 1. (a) Schematic of the non-chiral lattice unit; (b) Steady-state FE analysis of the non-chiral lattice unit; (c) LPM of the non-chiral lattice unit; (d) LPM of the diatomic non-chiral chain; (e) Band structure of the diatomic non-chiral chain computed using the LPM and the FEM. The torsional-mode energy fraction is color-mapped in the FEM results according to the torsional polarization factor.

[30–33], graded configuration [34–37], nonlinear resonators [38–41], and hybrid Bragg-resonant band gaps [42–45] have been explored to broaden attenuation bands. Despite these advances, complex resonator designs substantially increase fabrication complexity, and the trade-off among lightweight, compactness, high stiffness, and broadband low-frequency attenuation remains a major challenge.

Compression-torsion coupled chiral metamaterials (chiral metamaterials, for short), capable of converting axial translational loads into torsional motion, were first proposed in 2017 [46] and offer a promising route for broadband low-frequency wave control. The compression-torsional coupling effect introduces an additional rotational inertia, effectively amplifying the equivalent mass and significantly lowering band-gap onset frequencies [47–50]. The resulting band gaps have widths and attenuation levels comparable to those of BS and LR gaps, respectively [51–53]. Existing studies on chiral metamaterials fall into two broad categories. The first focuses on accurate modeling, including beam- or rod-based derivations of strain-torsion relations in chiral ligaments [54,55], derivations of coupling coefficients that account for large ligament deflections [56], and lumped-parameter models formulated via Lagrangian methods [57,58]. However, neglect of the coupled dynamic stiffness induced by ligament deformation generally restricts these models to predicting local single-mode behaviour and reduces their accuracy at higher frequencies. To this end, the finite element method [59,60] and the extended spectral element method [61,62] have been developed to capture the synergistic effects of rigid-flexible interaction and compression-torsion coupling.

The second category concerns band gap formation and wave propagation mechanisms. Drawing inspiration from tacticity in polymer science [63], isotactic and syndiotactic arrangements have been used to describe identical and opposite chirality orientations of adjacent units, which strongly affect the dynamic responses without altering static mass and stiffness [64–66]. Recent studies further indicate that inertia amplification, although beneficial for low-frequency broadband attenuation, is not the fundamental origin of band gaps [67]. Instead, a Thomson-scattering-like mechanism, associated with changes in modal polarization and the resulting destructive interference, has been proposed [67,68]. Compression-torsion coupling band gaps can also be combined with bending-shear coupling to achieve an omnidirectional wide band gap [57,69]. Furthermore, tacticity-induced local non-periodicity gives rise to novel wave phenomena. For instance, topological design strategies have enabled low-frequency torsional topologically protected interface states at interfaces between chiral metamaterials [70,71], and further studies on isotactic and syndiotactic configurations have revealed two distinct types of interface states [72]. Defect engineering via local geometry modulation has been shown to generate fully polarized defect states that respond to low-frequency orthogonal excitations, facilitating three-dimensional low-frequency energy harvesting [73]. Overall, by coupling translational and torsional wave motions, chiral metamaterials open new opportunities for broadband, low-frequency vibration suppression and multifunctional wave manipulation.

In this work, a defective chiral metamaterial capable of broadband low-frequency vibration attenuation through a virtual local resonance mechanism is proposed. The metamaterial is constructed from an isotactic arrangement of chiral unit cells, in which defects that remove chirality are introduced by embedding vertical rods. Unlike previous studies on defect metamaterials, which primarily aim to generate spatially localized modes within pre-existing band gaps and tailor defect states with multiple [74,75] or low-frequency characteristics [76–78], the present study reveals that chirality-removed defects induce an interface impedance mismatch within an isotactic lattice and thereby trigger a mode transition. This transition converts a propagating global longitudinal wave into a localized torsional resonance. As a result, a band gap emerges due to the strong attenuation of longitudinal energy under localized resonance. Similar to conventional LR band gaps, the resulting band gap enables efficient vibration suppression and flexible subwavelength wave manipulation. However, unlike traditional LR mechanisms that rely on periodically distributed physical resonators oscillating out of phase with the host structure, the proposed mechanism requires only a few defect units, which act as a virtual (equivalent) local resonator through mode transition. This feature effectively reconciles the inherent trade-offs of conventional approaches among broadband attenuation, small lattice constants, and lightweight design. Accordingly, we therefore refer to this gap as a virtual locally resonant band gap, where “virtual” emphasizes the absence of a physical resonator. In the following, the dynamic characteristics of the VLR band gap are systematically investigated through theoretical analysis, numerical simulations, and experimental validation.

This paper is organized as follows. Section 2 introduces theoretical models of non-chiral and chiral diatomic lattices, focusing on the effects of chirality orientation on mode transitions and dynamics. Section 3 presents the design of the defective chiral metamaterial, elucidates the VLR band-gap formation mechanism, and discusses its similarities to and differences from conventional local resonance. The superior broadband low-frequency performance is further demonstrated through parametric analysis and a graded configuration example. Section 4 experimentally

Table 1
Material and geometric properties of the metamaterial lattice.

D_m (cm)	h_m (cm)	$\overline{D}$(cm)	θ_a (°)	θ_c (°)	d (cm)	h (cm)	E (Gpa)	ρ (kg/m^3)	ν
6	0.8	3	90	45	0.36	3	2.4e9	1300	0.41

validates the numerical results and confirms the VLR band gap. Section 5 concludes the paper.

2. Dynamics of non-chiral and chiral lattices

This study demonstrates how an isotactic lattice containing a chirality-removed defect induces a VLR band gap. Before delving into this mechanism, this section reviews the wave characteristics of non-chiral and chiral lattices using lumped-parameter models (LPMs) and finite element models (FEMs). Two aspects are briefly summarized: (1) the compression-torsion coupling inherent to chiral lattices and its tendency to lower modal frequencies; and (2) the concept of mode transition and its influence on wave propagation.

2.1. Non-Chiral lattice characteristics

The non-chiral lattice unit is shown in Fig. 1(a). It comprises two discs (top and bottom) connected by four vertically aligned rods that are symmetrically arranged around the central axis. The spacing between adjacent rods is denoted as $\overline{D}$, leading to the diameter of the circular loop$D = \sqrt{2}\overline{D}$. The rod diameter is d. Other geometric parameters are labeled in Fig. 1(a). The slender rods are modeled as elastic elements able to undergo longitudinal extension/compression and torsional motion. Bending and higher-order vibration modes are neglected. The discs are treated as rigid bodies. The COMSOL result in Fig. 1(b) shows that, when a prescribed displacement along the z-axis is applied to the top disc while the bottom block is fixed, the response is essentially axial. For analytical convenience, the non-chiral unit is idealized by a lumped-parameter model shown in Fig. 1(c), consisting of a mass m, a translational stiffness k_a, and a torsional stiffness τ_a. The effective stiffness of the vertical rod can be estimated by [54]:

$$\begin{cases} k_a = \dfrac{\pi n E d^2}{4l} \\ \tau_a = \dfrac{3\pi n D^2 E d^4}{16l\left[4l^2 + 6\lambda(1+\nu)d^2\right]} + \dfrac{\pi n E d^4}{64(1+\nu)l}, \end{cases} \tag{1}$$

where n denotes the number of rods, E and ν represent the Young's modulus and Poisson's ratio of the rods, respectively. l is the rod length (equal to h in the non-chiral unit). The correction factor $\lambda = 10/9$

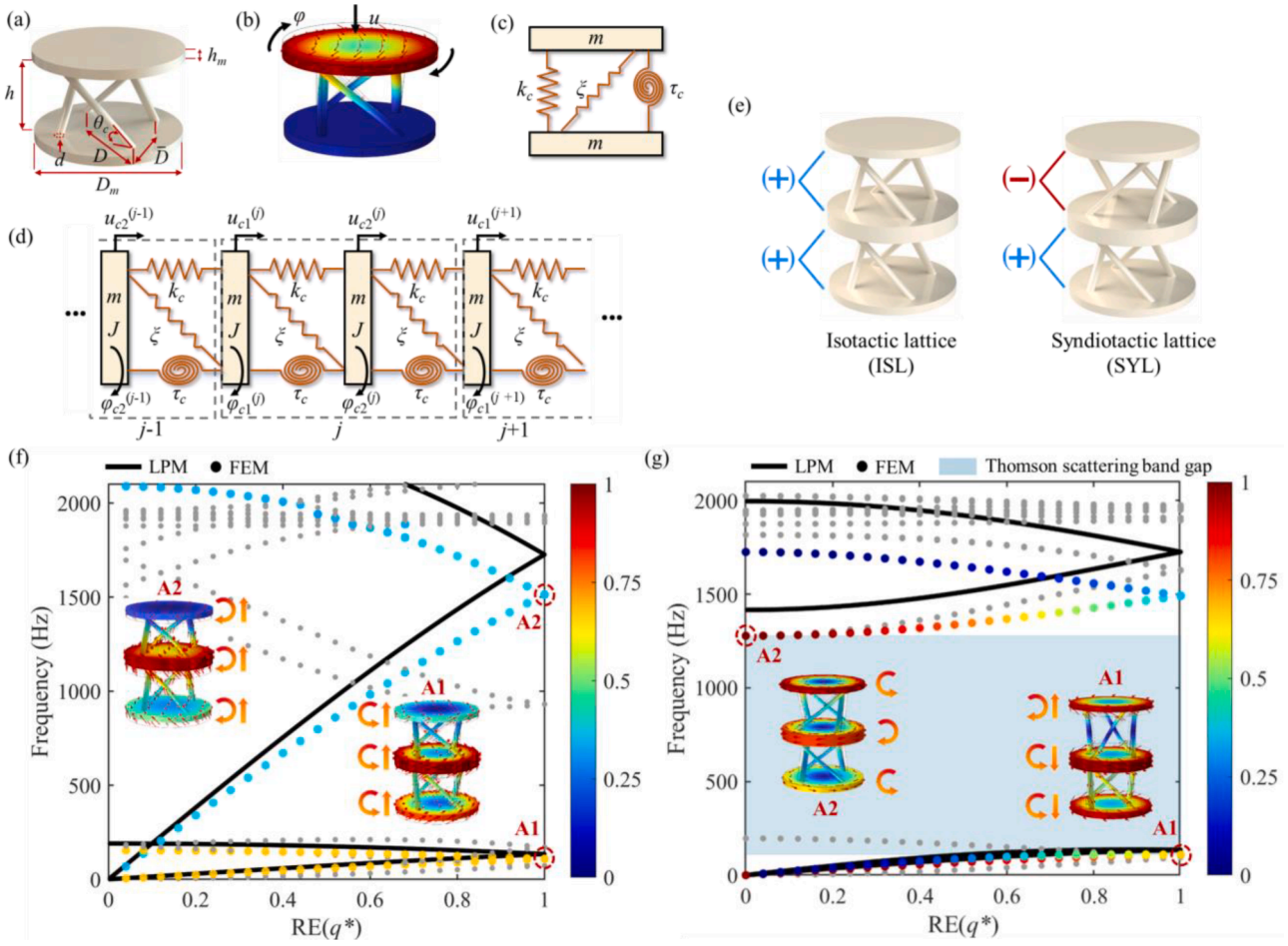

Fig. 2. (a) Schematic of the chiral lattice unit; (b) Steady-state FE analysis of the chiral lattice unit; (c) LPM of the chiral lattice unit; (d) LPM of the diatomic chiral chain; (e) Schematics of the isotactic and syndiotactic lattices. The symbols "+" and "-" indicate left-hand and right-hand chirality, respectively; (f) Band structure of the ISLs computed using the LPM and the FEM; (g) Band structure of the SYLs computed using the LPM and the FEM. The blue shaded region denotes the band gap induced by elastic Thomson scattering.

accounts for the inhomogeneous shear force distribution along the rod's cross-section. Eq. (1) is derived based on the Euler-Bernoulli beam theory and is valid under the geometric conditions $l/d \geq 10$ and $D/d \geq 10$.

To clarify differences in wave propagation between non-chiral and chiral configurations, band structures are computed from both the LPM and FE simulations. The diatomic nonchiral chain is considered, and its LPM under axis and torsional excitation about the z-axis is shown in Fig. 1(d). The equation of motion for the j-th unit cell is derived as follows:

$$m\frac{\mathrm{d}^2 {u_{a,1}}^{(j)}}{\mathrm{d}t^2} = k_a\left({u_{a,2}}^{(j)} - {u_{a,1}}^{(j)}\right) + k_a\left({u_{a,2}}^{(j-1)} - {u_{a,1}}^{(j)}\right), \tag{2}$$

$$J\frac{\mathrm{d}^2 {\varphi_{a,1}}^{(j)}}{\mathrm{d}t^2} = \tau_a\left({\varphi_{a,2}}^{(j)} - {\varphi_{a,1}}^{(j)}\right) + \tau_a\left({\varphi_{a,2}}^{(j-1)} - {\varphi_{a,1}}^{(j)}\right), \tag{3}$$

$$m\frac{\mathrm{d}^2 {u_{a,2}}^{(j)}}{\mathrm{d}t^2} = k_a\left({u_{a,1}}^{(j)} - {u_{a,2}}^{(j)}\right) + k_a\left({u_{a,1}}^{(j+1)} - {u_{a,2}}^{(j)}\right), \tag{4}$$

$$J\frac{\mathrm{d}^2 {\varphi_{a,2}}^{(j)}}{\mathrm{d}t^2} = \tau_a\left({\varphi_{a,1}}^{(j)} - {\varphi_{a,2}}^{(j)}\right) + \tau_a\left({\varphi_{a,1}}^{(j+1)} - {\varphi_{a,2}}^{(j)}\right), \tag{5}$$

where m and $J = 1/2m(D_\mathrm{m}/2)^2$are the mass and rotational inertia of the disc. u_a and φ_a denote the translational and torsional displacements of the non-chiral unit, respectively. The subscripts 1 and 2 refer to the first and second sublattices within each unit cell. The geometric and material parameters listed in Table 1 are used, from which the translational and torsional stiffnesses are calculated as $k_a = 3257.2$ kN/m, and $\tau_a = 17.18$ N·m/rad. According to Bloch's theorem, the harmonic wave solutions are assumed to have the form:

$$\begin{cases} {u_{a,n}}^{(j)} = U_{a,n}e^{i(jq-\omega t)} \\ {\varphi_{a,n}}^{(j)} = \Phi_{a,n}e^{i(jq-\omega t)} \end{cases}, \tag{6}$$

where $n = 1, 2$ indexes the sublattices, q is the Bloch wave vector, $U_{a,n}$ and $\Phi_{a,n}$ are complex amplitude coefficients. Substituting Eq. (6) into Eqs. (2)- (5) yields the standard matrix eigenvalue problem:

$$\left(\mathbf{K} - \omega^2\mathrm{M}\right)\mathbf{u} = \mathbf{0}. \tag{7}$$

Solving Eq. (7) yields the band structure $\omega(q)$ within the first irreducible Brillouin zone, as shown in Fig. 1(e). It is seen that the bands fold back into the irreducible Brillouin zone due to the diatomic chain, producing degenerate Dirac points [79,80] at the zone edges. The discrete markers indicate FEM results calculated by COMSOL Multiphysics 6.1. To highlight the mode polarization, we adopt the torsional polarization factor λ from [72], which quantifies the fraction of torsional energy in each mode as follows:

$$\lambda = \frac{\int_{V_d} J(|\varphi_z|)^2 dV_d}{\int_{V_d}\left[J(|\varphi_z|)^2 + m(|u_z|)^2\right]dV_d}, \tag{8}$$

where V_d is the volume of the discs in the unit cell, and u_z, φ_z are the translational and torsional displacement components along the z-axis. The torsional polarization factor λ, which ranges from 0 to 1, is mapped onto the band diagram using a colormap, with both translational and torsional modes colored according to their λ. Points in deep red indicate nearly pure torsional modes (i.e., $\lambda \approx 1$), and deep blue points correspond to nearly pure translational modes (i.e., $\lambda \approx 0$). In addition, to present the complete band structure, other irrelevant eigenmodes, such as bending or nonlinear deformation modes, are shown in gray. The pronounced red-blue separation shown in Fig. 1(e) confirms that translational and torsional motions are effectively decoupled in the non-chiral lattice. Mode shapes at the degenerate Dirac points A1 and A2 are presented as evidence of this decoupling, with arrows denoting the direction of motion.

2.2. Chiral lattice characteristics

Fig. 2(a) illustrates the chiral lattice unit, comprising two discs connected by four inclined rods arranged in a chiral configuration. Due to the slender geometry of the rods, the non-circular contact area at the rod-mass interface is negligible, and the rod diameter is taken as d. The angle between each rod and the horizontal plane of the disc is denoted as θ_c. Additional geometric relationships are labeled in Fig. 2(a). In contrast to the non-chiral design, the chiral geometry couples the orthogonal translational and torsional motions under axial and/or rotational loading, producing a compression-torsion coupling effect, as shown in the FEM result (Fig. 2(b)). Accordingly, the chiral unit is represented by the LPM in Fig. 2(c), where k_c, τ_c, and ξ are the translational stiffness, torsional stiffness, and the compression-torsional coupling coefficient, respectively. These parameters can be theoretically estimated as follows [54]:

$$\begin{cases} k_c = \dfrac{\pi n E d^2\left[4l^2\sin^2\theta_c + 3d^2\cos^2\theta_c + 6\lambda(1+\nu)d^2\sin^2\theta_c\right]}{4l\left[4l^2 + 6\lambda(1+\nu)d^2\right]} \\ \tau_c = \dfrac{\pi n E d^2\left[4l^2\cos^2\theta_c + 3d^2\sin^2\theta_c + 6\lambda(1+\nu)d^2\cos^2\theta_c\right]\left(D^2 - l^2\cos^2\theta_c\right)}{16l\left[4l^2 + 6\lambda(1+\nu)d^2\right]} \\ \xi = \dfrac{\pi n E d^2\left[4l^2 - 3d^2 + 6\lambda(1+\nu)d^2\right]\sin\theta_c\cos\theta_c\sqrt{D^2 - l^2\cos^2\theta_c}}{8l\left[4l^2 + 6\lambda(1+\nu)d^2\right]} \end{cases}. \tag{9}$$

The LPM of a diatomic chiral chain is depicted in Fig. 2(d), and the equation of motion for the j-th unit can be derived as [72]:

$$\begin{aligned} m\frac{\mathrm{d}^2 {u_{c1}}^{(j)}}{\mathrm{d}t^2} = {} & k_c\left({u_{c2}}^{(j)} - {u_{c1}}^{(j)}\right) + k_c\left({u_{c2}}^{(j-1)} - {u_{c1}}^{(j)}\right) + \xi_1\left({\varphi_{c2}}^{(j)} - {\varphi_{c1}}^{(j)}\right) \\ & + \xi_2\left({\varphi_{c2}}^{(j-1)} - {\varphi_{c1}}^{(j)}\right), \end{aligned} \tag{10}$$

$$\begin{aligned} J\frac{\mathrm{d}^2 {\varphi_{c1}}^{(j)}}{\mathrm{d}t^2} = {} & \xi_1\left({u_{c2}}^{(j)} - {u_{c1}}^{(j)}\right) + \xi_2\left({u_{c2}}^{(j-1)} - {u_{c1}}^{(j)}\right) + \tau_c\left({\varphi_{c2}}^{(j)} - {\varphi_{c1}}^{(j)}\right) \\ & + \tau_c\left({\varphi_{c2}}^{(j-1)} - {\varphi_{c1}}^{(j)}\right), \end{aligned} \tag{11}$$

$$\begin{aligned} m\frac{\mathrm{d}^2 {u_{c2}}^{(j)}}{\mathrm{d}t^2} = {} & k_c\left({u_{c1}}^{(j)} - {u_{c2}}^{(j)}\right) + k_c\left({u_{c1}}^{(j+1)} - {u_{c2}}^{(j)}\right) + \xi_1\left({\varphi_{c1}}^{(j)} - {\varphi_{c2}}^{(j)}\right) \\ & + \xi_2\left({\varphi_{c1}}^{(j+1)} - {\varphi_{c2}}^{(j)}\right), \end{aligned} \tag{12}$$

$$\begin{aligned} J\frac{\mathrm{d}^2 {\varphi_{c2}}^{(j)}}{\mathrm{d}t^2} = {} & \xi_1\left({u_{c1}}^{(j)} - {u_{c2}}^{(j)}\right) + \xi_2\left({u_{c1}}^{(j+1)} - {u_{c2}}^{(j)}\right) + \tau_c\left({\varphi_{c1}}^{(j)} - {\varphi_{c2}}^{(j)}\right) \\ & + \tau_c\left({\varphi_{c1}}^{(j+1)} - {\varphi_{c2}}^{(j)}\right), \end{aligned} \tag{13}$$

where u_c and φ_c are the translational and rotational displacements of the chiral unit. Compared to the non-chiral one, the chiral lattice exhibits two main advantages. First, torsional motion significantly increases the effective inertial mass of the unit cell through an inertia amplification effect, which lowers its natural frequencies. Second, compression-torsion coupling allows translational and torsional motions to interfere within certain frequency bands, producing band gaps. Importantly, the band gaps are highly sensitive to the chirality orientation. To be specific, Fig. 2(e) presents diatomic chiral lattices with different chirality arrangements. Following the concept of tacticity in polymer science, these configurations are classified as an isotactic lattice (ISL, for short) and a syndiotactic lattice (SYL) [65]. In an ISL (left panel of Fig. 2(e)), all unit cells share the same left-handed chirality, denoted by '+'. In contrast, in a SYL (right panel of Fig. 2(e)), the unit cells exhibit an alternating chirality sequence. Although ISLs and SYLs possess identical static mass and stiffness distributions, their dynamic responses differ markedly:

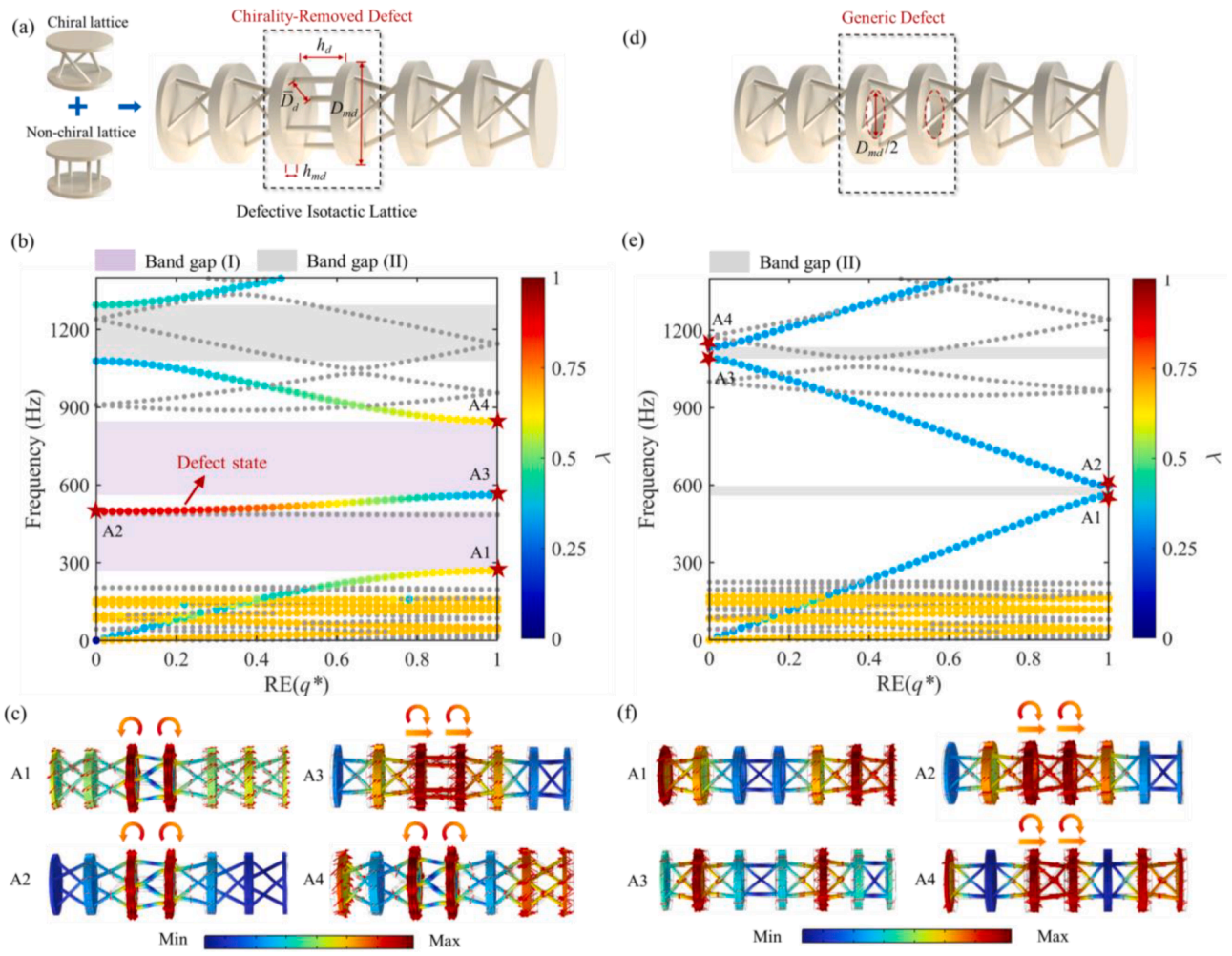

Fig. 3. (a) Schematic of the DISL; (b) Band structure of the DISL computed using FEM. Pink shading highlights the VLR band gap, and the gray shading denotes the topological band gap. Band-edge modes A1-A4 are marked with red pentagrams; (c) Mode shapes corresponding to A1-A4 in (b), where A1, A2, and A4 show that the left and right mass blocks of the defect unit undergo pure, out-of-phase torsional rotation; (d) Schematic of an ISL supercell with an alternative defect (conterpart); (e) Band structure of the supercell conterpart computed using FEM. Neither mode transition nor a VLR band gap is observed. Topological band-edge modes A1-A4 are marked by red pentagrams; (f) Mode shapes corresponding to A1-A4 in (e), showing no torsional local resonance in the defect unit.

SYLs are known to produce wide low-frequency band gaps under axial or torsional excitation, a phenomenon that has been attributed to an elastic Thomson scattering mechanism [68].

To illustrate this, band structures of the ISL and SYL are computed from Eqs. (10)- (13) and shown in Fig. 2(f) and (g), respectively. Using the geometric and material parameters in Table 1, the system's translational and torsional stiffnesses are calculated as $k_c = 1157.7$ N/m and $\tau_c = 262.1$ N·m/rad. The compression-torsion coupling coefficient is $\xi = 17{,}182.2$ N/rad for the left-hand unit and $\xi = -17{,}182.2$ N/rad for the right-hand unit. Compared with the results in Fig. 1(e), the dispersion curves shift to lower frequencies, which results from inertia amplification induced by compression and torsion coupling. The FEM results in Fig. 2(f), colored by the torsional polarization factor, show that the dispersion branches of the ISL no longer correspond to purely single character modes because translational and torsional motions are coupled by ξ. Specifically, the modal energy distribution varies between branches: the low-frequency branches are dominated by torsional motion with $\lambda \approx 0.67$, whereas the higher-frequency branches are dominated by translational motion with $\lambda \approx 0.32$. Mode shapes at the degenerate Dirac points A1 and A2, plotted as insets in Fig. 2(f), illustrate this behavior and indicate that adjacent units oscillate in phase.

By contrast, the SYL exhibits a pronounced evolution of modal polarization along the second and third dispersion branches, as shown in Fig. 2(g). Specifically, the second branch evolves from a translation-dominated mode at RE(q^*) = 0 ($\lambda \approx 0$) to a torsion-dominated mode at RE(q^*) = 1 ($\lambda \approx 0.67$), while the third branch transforms from a torsion-dominated mode at RE(q^*) = 0 ($\lambda \approx 1$) to a translation-dominated mode at RE(q^*) = 1 ($\lambda \approx 0.33$). This phenomenon, referred to as a mode transition [81], stems from the change in chirality, which reverses the sign of the compression-torsion coupling coefficient ξ. The sign reversal flips the direction of transmitted forces/torques between neighboring units, substantially changing the relative contributions of translational and torsional components and thereby producing the observed mode transition. Insets A1 and A2 in Fig. 2(g) show the mode shapes at the band-edge points and confirm that neighboring units oscillate out of phase due to the reversal forces/torques. Notably, a band gap (shaded in blue) emerges from 110.5 Hz to 1278.6 Hz, lying between two branches that undergo pronounced mode transitions between longitudinal translation and torsion. Previous studies have interpreted this gap in terms of an elastic Thomson-scattering [68]: secondary mode transitions induced by units of reversed chirality generate oppositely phased motions that destructively interfere. By contrast, the ISL does not exhibit this band gap because all its units share the same chirality.

In summary, although the ISL and SYL have identical stiffness and mass per unit cell, their distinct chiral topologies give rise to different motion couplings, and the alternating chiral orientation leads to mode

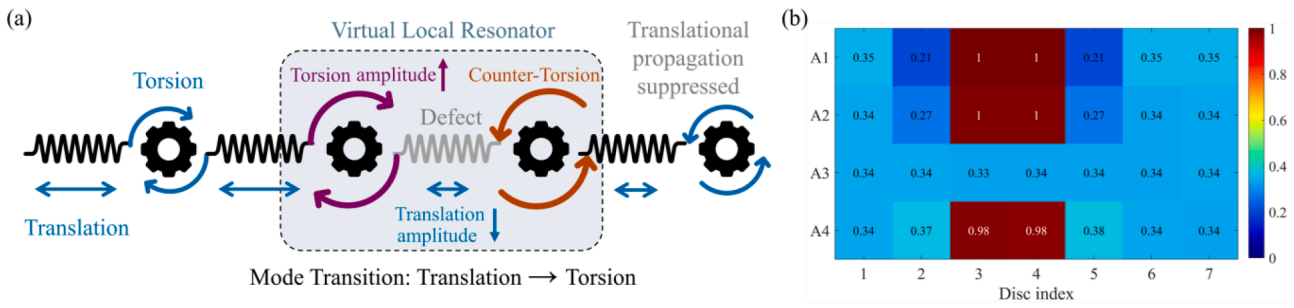

Fig. 4. (a) Schematic depiction of the virtual local resonator induced by mode transition; (b) Torsional energy fraction λ of mass blocks 1–7 in the DISL for modes A1-A4.

transitions as the wavenumber varies. In what follows, we introduce chirality-removed defects into the ISL and exploit these mode transitions to create a newly formed band gap, referred to as a virtual locally resonant band gap.

3. Virtual locally resonant band gap in chiral lattices

Defect engineering deliberately introduces geometric or material imperfections into periodic structures. By breaking spatial symmetry, such defects create localized energy traps within band gaps, thereby confining and amplifying wave motion. In this section, we introduce chirality-removed defects into the chiral lattice with two objectives: (1) to elucidate the formation mechanism of the VLR band gap; and (2) to verify its local resonance characteristics.

3.1. VLR band-gap formation via mode transitions

A six-unit ISL supercell containing a chirality-removed defect is considered, which is formed by assembling left-handed chiral units with a non-chiral unit placed at the third position, as shown in Fig. 3(a). This defect unit is characterized by several geometric parameters, i.e., D_{md}, $\overline{D}_d$, h_{md}, and h_d, as shown in Fig. 3(a). In this section, these parameters are set equal to those of the non-chiral unit listed in Table 1. The vertical rods in the defect unit eliminate compression-torsion coupling (i.e., $\xi = 0$) and slightly increase its translational and torsional stiffness compared with the inclined-rod units. Note that introducing this defect creates an interface impedance mismatch within the periodic chain. For brevity, the ISL containing chirality-removed defects is denoted as defective isotactic lattice (DISL, for short). An infinite periodic model of the DISL is established using COMSOL. Bloch boundary conditions are imposed on the faces of the discs of units 1 and 6 to obtain the band structure. The polarization factor defined in Eq. (8) is overlaid on the band diagram as a colormap to visualize modal polarization along the dispersion branches, while irrelevant modes are displayed in gray. The resulting band structure is plotted in Fig. 3(b). In the low-frequency range ($\approx$ 0 −158.9 Hz), the bands remain predominantly torsional ($\lambda \approx 0.68$), consistent with the ISL bands shown in Fig. 2(f). Notably, upon introduction of the defect, several dispersion branches undergo a pronounced evolution in modal polarization, similar to the behavior observed in the SYL. Interleaved among these branches are two distinct band gaps, labeled (I) and (II) and shaded pink and gray, respectively, even though the uniform ISL is typically not expected to support band gaps. It should be noted that the gray branches appearing within band gap (II) do not affect its formation. As noted earlier, these branches correspond to irrelevant modes, which cannot be excited under longitudinal/torsional loading. Consequently, they do not participate in wave propagation under the excitation conditions considered in this study. According to the band folding theory, band gap (II) can be identified as a topological band gap. It stems from supercell-induced Brillouin zone folding, which creates degenerate Dirac points. When the defect is introduced, the symmetry of the ISL is broken, the degeneracy is lifted, and a topological band gap consequently opens [82].

To clarify the physical origin of band gap (I), the band-edge mode shapes are examined. Fig. 3(c) plots the band-edge mode shapes labeled A1-A4 at RE(q^*) = 0 or 1. Modes A1 and A4 show that units away from the defect undergo compression-torsion coupled motion, with neighbouring units oscillating in phase. By contrast, the defect unit exhibits pure torsional motion with opposite phase and significantly larger amplitude. This indicates that a mode transition occurs at the defect, causing it to behave like a resonator that undergoes large-amplitude and out-of-phase motion. In addition, a relatively flat branch appears inside the band gaps (I). Its edge modes A2 and A3 show strong energy localization at the defect unit, while the rest of the chain remains nearly motionless, indicating that this branch is a defect band [83]. This band arises because the defect breaks the spatial periodicity, producing a localized passband within the band gap, where waves at specific frequencies form standing waves that concentrate energy at the defect unit [83]. The modes A2 and A3 are referred to as defect states. However, unlike conventional defect bands, this defect branch also exhibits modal polarization evolution across the irreducible Brillouin zone. Specifically, in mode A2, the two discs within the defect unit perform torsional motions with opposite phase, forming a dipole-like defect pattern [84], whereas in mode A3, the two discs oscillate in a translational manner, resulting in a monopole-like defect pattern [85].

From the above observations, a key conclusion can be drawn: the formation mechanism of band gap (I) in the DISL arises from a local resonance mechanism induced by mode transition. Specifically, removing the local unit's chirality introduces an impedance mismatch at the interface. Similar to the SYL configuration in subSection 2.2, this impedance mismatch triggers a mode transition within the coupled translational-torsional mode at the defect unit. As a result, the translational component of the incident wave is completely converted into torsional motion. As illustrated by the modal shapes A1, A2, and A4 in Fig. 3(c), the discs in the defect unit undergo pronounced out-of-phase rotational motion. This process, in which energy associated with one degree of freedom is locally transformed into another, closely resembles the local resonance mechanism [86]. However, unlike conventional locally resonant systems that require physical resonators to extract energy from the host structure, the local resonance of the DISL relies on mode transition caused by impedance mismatch under chirality removal. Consequently, the defect unit itself effectively functions as a virtual local resonator: it absorbs translational energy from the host lattice and converts it into localized torsional motion, strongly suppressing wave transmission and thereby opening a band gap (I). It is important to stress a subtle but crucial distinction relative to conventional designs. In classical LR metamaterials, resonators are placed off the main load path to siphon transmitted energy. In the DISL, the virtual local resonator is geometrically located on the translational load path, yet because the incident translational energy is converted into a localized torsional DOF that couples weakly back into the translational propagation channel, the defect behaves dynamically as if it were off-path.

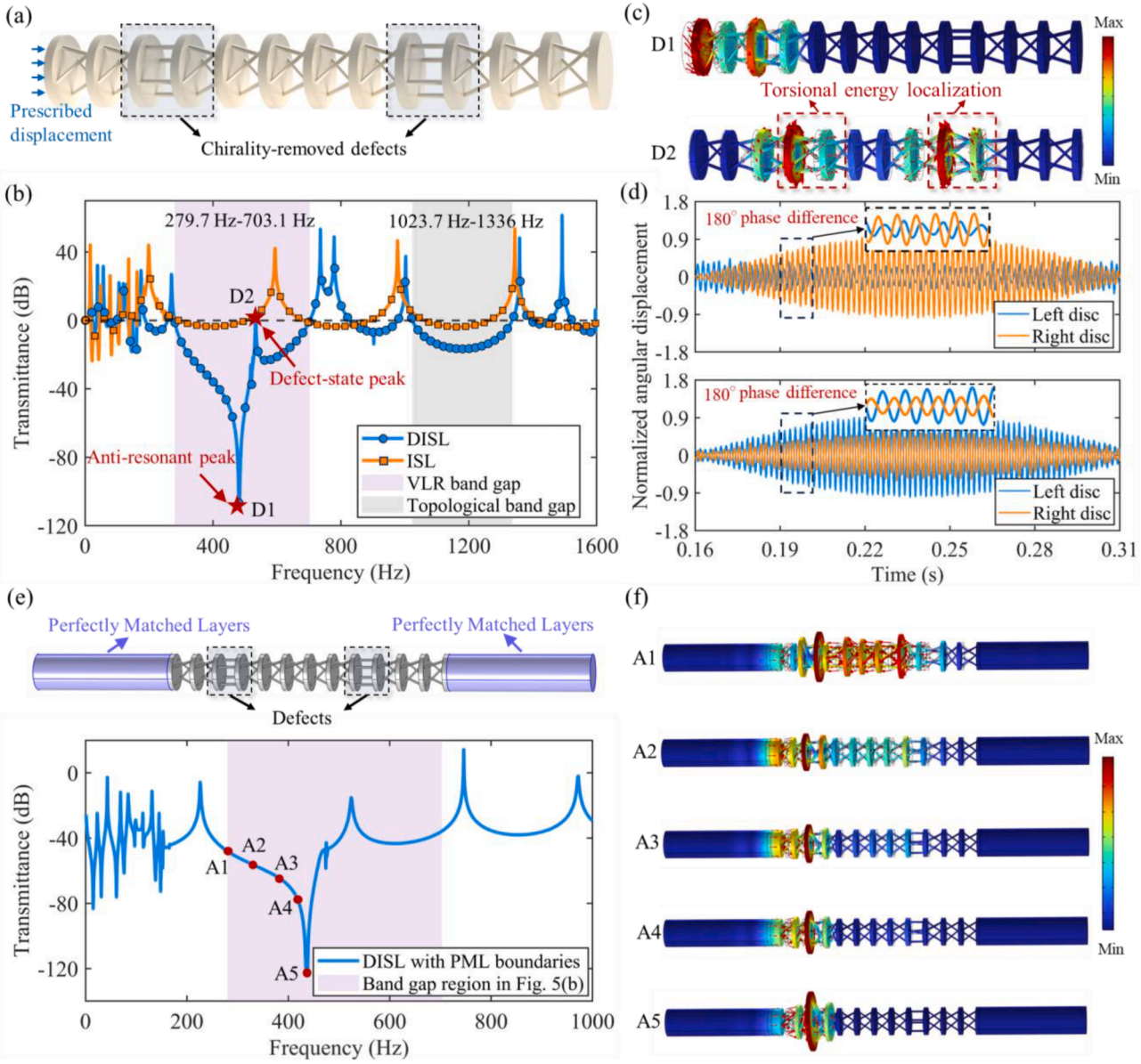

Fig. 5. (a) Schematic of the DISL with 12 units; (b) Comparison of the transmittances for the DISL and ISL; (c) Mode shapes corresponding to the anti-resonances and defect-state peaks marked by red pentagrams D1 and D2 in (b). Mode D2 clearly shows torsional energy localization at the defect unit; (d) The normalized angular displacements of the left and right discs of the first defect unit (upper panel) and the second defect unit (lower panel) under harmonic excitation, where the two discs exhibit a 180-degree phase difference; (e) Configuration of the 12-unit DISL with PMLs and the corresponding Transmittance; (f) Mode shapes corresponding to A1-A5 in (e).

It should be noted that without a local chirality change, band gap (I) does not emerge, as the required mode transition cannot be triggered. To demonstrate this, Fig. 3(d) presents an ISL supercell containing an alternative defect unit composed of rings and inclined ligaments. The inner diameter of the ring is set to $1/2D_{md}$, while all other geometric parameters are identical to those of the pristine ISL unit. Although this defect alters the mass and rotational inertia of the unit cell, it does not change the chirality orientation or the compression-torsion coupling coefficient. The corresponding band structure, shown in Fig. 3(e), shows that no mode transition occurs along the branches associated with translational and torsional modes. Instead, only two narrow topological band gaps (shaded in gray) open at degenerate Dirac points. Fig. 3(f) further displays the edge-mode shapes at the boundaries of topological band gaps, labeled A1-A4 at RE(q^*) = 0 or 1, from which no torsional resonant behavior is observed in the defect unit.

Fig. 4(a) graphically illustrates the formation process of the mode transition and band gap (I) in the DISL. Under the action of the virtual local resonator, the torsional vibration amplitude is significantly amplified, whereas the translational vibration is correspondingly reduced, resulting in effective vibration suppression of the system. Additional support for this interpretation is obtained by evaluating the torsional-energy fraction λ for each disc of the DISL in modes A1-A4 using Eq. (8), where the total-volume term is replaced by the corresponding volume integral over each disc, as shown in Fig. 4(b) (x-axis: disc index from left to right). It is observed that, for modes A1, A2, and A4, the discs within the defect unit exhibit nearly pure torsional motion ($\lambda \approx 1$). This confirms that, under the mode transition mechanism, the energy of the incoming translational wave is fully transformed into torsional energy and becomes localized within the defect unit. Although mode A3 at RE(q^*) = 1 is not torsion-dominated within the defect unit due to a polarity change, it does not play a central role in the formation of this band gap. Since band gap (I) in the DISL arises from these modal

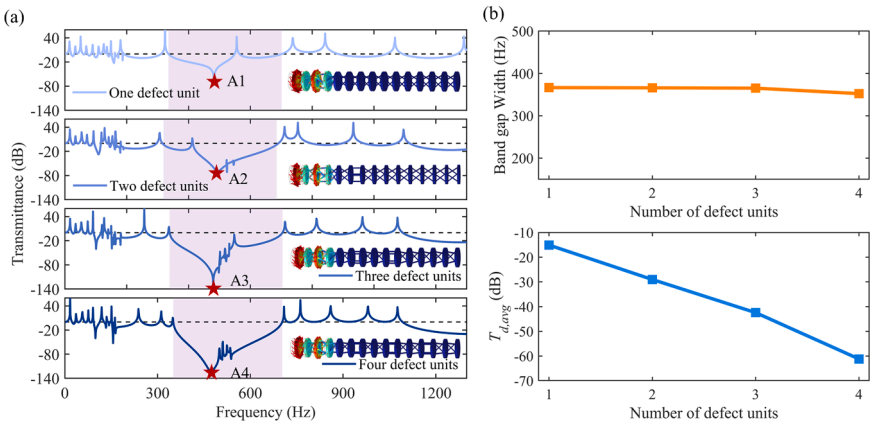

Fig. 6. (a) Transmittance variation of the 14-unit DISL with different numbers of defect units. Insets show the mode shapes of the anti-resonance peaks corresponding to A1-A4; (f) Variations of the band gap bandwidth and the average transmittance $T_{d,avg}$ as functions of the number of defect units.

transitions in the absence of a physical resonator and therefore differs fundamentally from conventional LR band gaps, we denote it a virtual locally resonant (VLR) band gap.

In the following subsections, we characterize the VLR band gap from three perspectives: (1) transmission behavior, (2) tunability with resonance parameters, and (3) the contribution of individual virtual local resonators to vibration attenuation. By comparing these features with those of conventional LR band gaps, we further demonstrate that the observed gap arises from a local resonance mechanism and emphasize the unique advantages of the VLR approach.

3.2. *Analysis of transmission behavior*

The transmission characteristics of a finite structure play an important role in evaluating band gap behavior. To demonstrate the transmission characteristics of the VLR band gap, a 12-unit DISL model is constructed first, in which the 3rd and 9th units serve as defect units, as shown in Fig. 5(a). To accurately identify the band gap boundaries, damping is neglected. The other geometric and material parameters are kept consistent with those used in the aforementioned infinite DISL model. A prescribed translational displacement U_{in} along the z-axis is applied to the leftmost disc. The transmitted displacement U_{out} is obtained by averaging the z-axis displacement over the rightmost disc, and the displacement transmittance is calculated by $T_d = 20\log_{10}(U_{\text{out}}/\,U_{\text{in}})$. Fig. 5(b) shows the transmittance of the 12-unit DISL. For comparison, the FEM result for a 12-unit ISL is also plotted in Fig. 5(b). The results show that the DISL exhibits two band gaps, a VLR band gap (shaded in pink) and a topological band gap (shaded in gray), whereas no band gaps are observed in the ISL. The transmittance response within the VLR band gap is characterized by deep minima and a pronounced anti-resonance feature (labeled D1), which closely resembles the spectral signature of traditional LR band gaps. Specifically, in typical LR systems, strong coupling between local resonators and the host structure produces deep valleys in the transmittance spectrum, corresponding to substantial vibration suppression [87]. The anti-resonance at D1 is generally tied to the resonator's natural frequency, where destructive interference is strongest and attenuation reaches its maximum [88]. This deep transmittance valley, therefore, confirms the locally resonant character of the VLR band gap. In addition, the peaks labeled D2 in Fig. 5(b) correspond to a defect-state peak. The mode shapes associated with D1 and D2 are shown in Fig. 5(c). At the anti-resonant peak (D1), the wave energy is rapidly attenuated when passing through the first defect unit due to the torsional local resonance, effectively blocking wave transmission. At the defect state (D2), the wave cannot propagate through the DISL, and the energy is strongly localized around the two defect units. By comparison, the transmittance profile associated with the topological band gap in Fig. 5(b) is relatively smooth, without pronounced anti-resonance features, and exhibits weaker attenuation. This behavior is consistent with the characteristics of topological band gaps reported in previous studies [89]. For a clearer illustration of the torsional resonance occurring at the defect units, the time-domain rotational responses of the left and right discs in the two defect units are calculated about the z-axis. Specifically, an exponentially-ramped displacement $d(t) = A\left(1 - e^{-t/\tau}\right)\sin(\omega t)$is applied to the leftmost disc of the DISL along the z-axis, where $\omega = 2\pi \times 534$ corresponds to the angular frequency of the defect state D2 shown in Fig. 5(b). The normalized angular displacements of the target discs are presented in Fig. 5(d). As shown, the left and right discs in both the first (upper panel) and second (lower panel) defect units exhibit a phase difference of approximately 180° under the defect-state excitation, confirming the occurrence of torsional resonance.

It is known that waves inside the band gap are evanescent, and their mode shapes exhibit decay of amplitude in space, providing a clear signature of band gap behavior. To better approximate the band gap conditions of an infinite periodic medium, perfectly matched layers (PMLs) are introduced to both ends of the configuration shown in Fig. 5(e), where they absorb outgoing waves and suppress boundary reflections. This approach is commonly used to approximate a finite structure as an effectively infinite periodic system [90–92]. Fig. 5(f) plots the transmittance measured at the rightmost unit of the DISL with PMLs. The band gap region calculated in Fig. 5(b) is highlighted in pink for reference. Compared with the case without PMLs, i.e., Fig. 5(b), the overall trend of the transmittance profile is preserved, while the absolute magnitude is reduced. This reduction is expected because the probe point is positioned in proximity to the PML. The presence of the absorbing layer continuously extracts wave energy near the boundary.

The frequency points A1-A5 in Fig. 5(e) span from the band-edge region to the antiresonance peak, and their corresponding mode shapes are plotted in Fig. 5(f). At A1, the wave propagates through a substantial portion of the structure and exhibits maximum amplitudes at the first and second defect units. This occurs because, although the defect units act as virtual local resonators during the mode transition and attenuate the transmitted energy, the operating frequency at A1 is slightly detuned from their equivalent resonance, resulting in relatively weak attenuation. As the frequency approaches A5, the transmitted wave exhibits increasingly rapid attenuation after passing the first defect unit, indicating the progressively enhanced suppression effect of the virtual local resonator. At the antiresonance point A5, the transmitted energy is concentrated at the first defect unit and is almost completely attenuated thereafter. These observations are consistent with the typical behavior of LR metamaterials. For the subsequent investigation of transmission characteristics relevant to finite-length, the remainder of the study is carried out without applying PML.

Another characteristic of conventional LR band gaps is that multiple

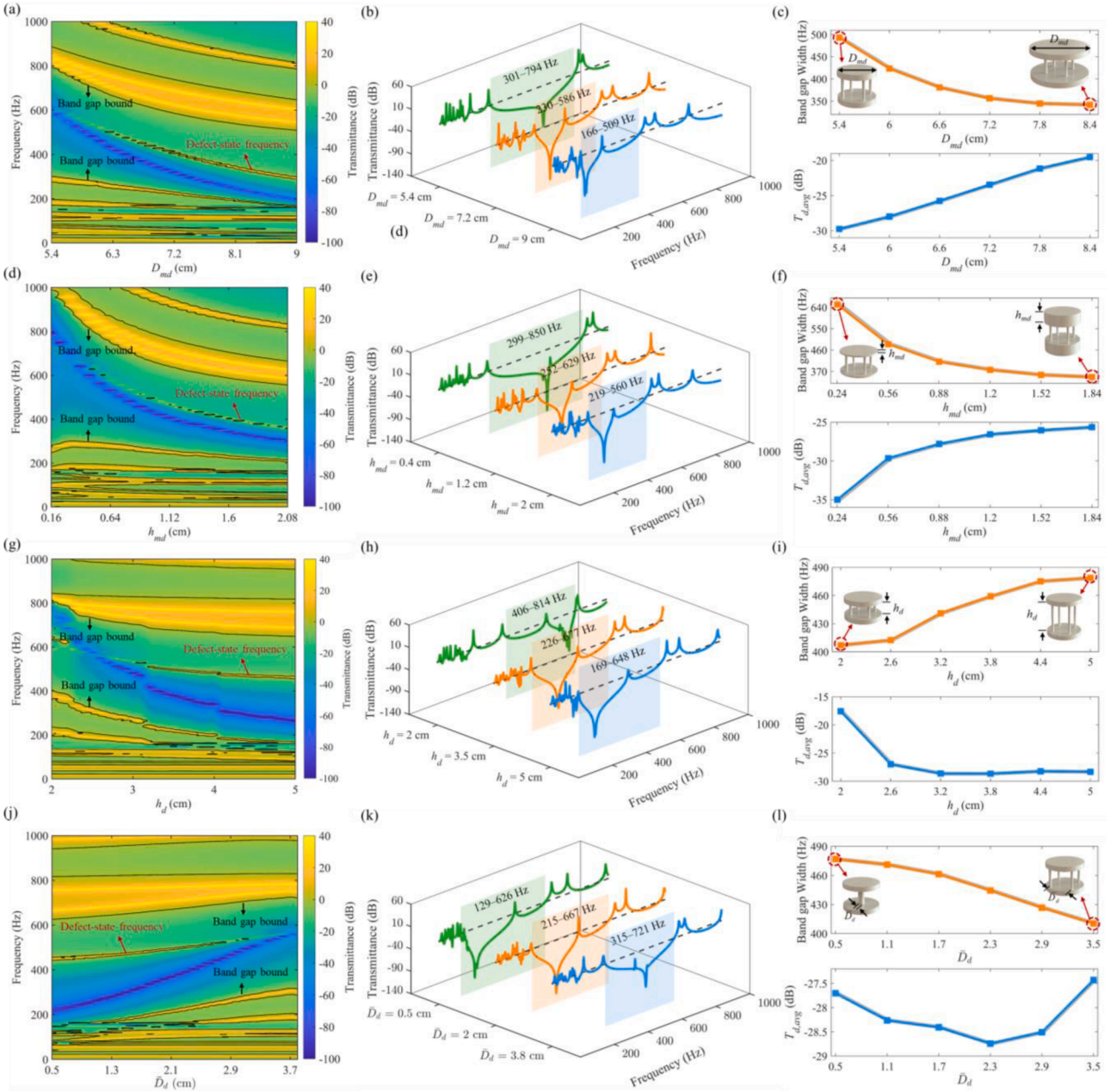

Fig. 7. (a, d, g, j) Heatmap of the displacement transmittance of the 12-unit DISL for varying D_{md}, h_{md}, h_d, and $\overline{D}_d$, respectively. The $T_d = 0$ dB contour is outlined with black lines to highlight the band gap region; (b, e, h, k) Transmittance slices corresponding to (a, d, g, j) at several representative parameter values. The VLR band gap is indicated by colored shading with the corresponding frequency range; (c, f, i, l) Variations of the band gap bandwidth and the average transmittance $T_{d,avg}$ as functions of D_{md}, h_{md}, h_d, and $\overline{D}_d$, respectively.

resonators are required to achieve noticeable attenuation, typically more than six according to previous studies [93]. Increasing the number of resonators has little influence on the band gap boundary and bandwidth, but markedly enhances the attenuation level [93,94]. To examine the dependence of the proposed VLR band gap on resonator density, Fig. 6(a) compares the transmittances of a 14-unit DISL with different numbers of virtual local resonators (i.e., defect units). The four subplots in Fig. 6(a), from top to bottom, correspond to configurations with one (the 3rd unit), two (the 3rd and 6th units), three (the 3rd, 6th, and 9th units), and four (the 3rd, 6th, 9th, and 12th units) defect units, respectively. The mode shapes at the anti-resonance frequencies for each case are labeled A1-A4 and shown as insets in Fig. 6(a). The results indicate that increasing the number of virtual local resonators does not significantly affect the band gap boundary or bandwidth (shaded in pink). However, the attenuation strength within the band gap is progressively enhanced as the number of virtual local resonators increases, which is consistent with the behavior of conventional LR systems [93]. For quantitative evaluation, Fig. 5(f) presents the variations in the band gap bandwidth and the average transmittance $T_{d,avg}$ within the VLR band gap, providing clearer evidence of this trend. It is noteworthy that a pronounced VLR band gap already emerges when only two virtual local resonators are introduced, which is substantially fewer than the number typically required for conventional LR band gaps. Nevertheless, it should be emphasized that the defect units must be embedded within the chiral lattice to function as virtual local resonators. As a result, unlike conventional LR metamaterials, where resonators can be densely arranged, adjacent defect units in the DISL must be separated by chiral units.

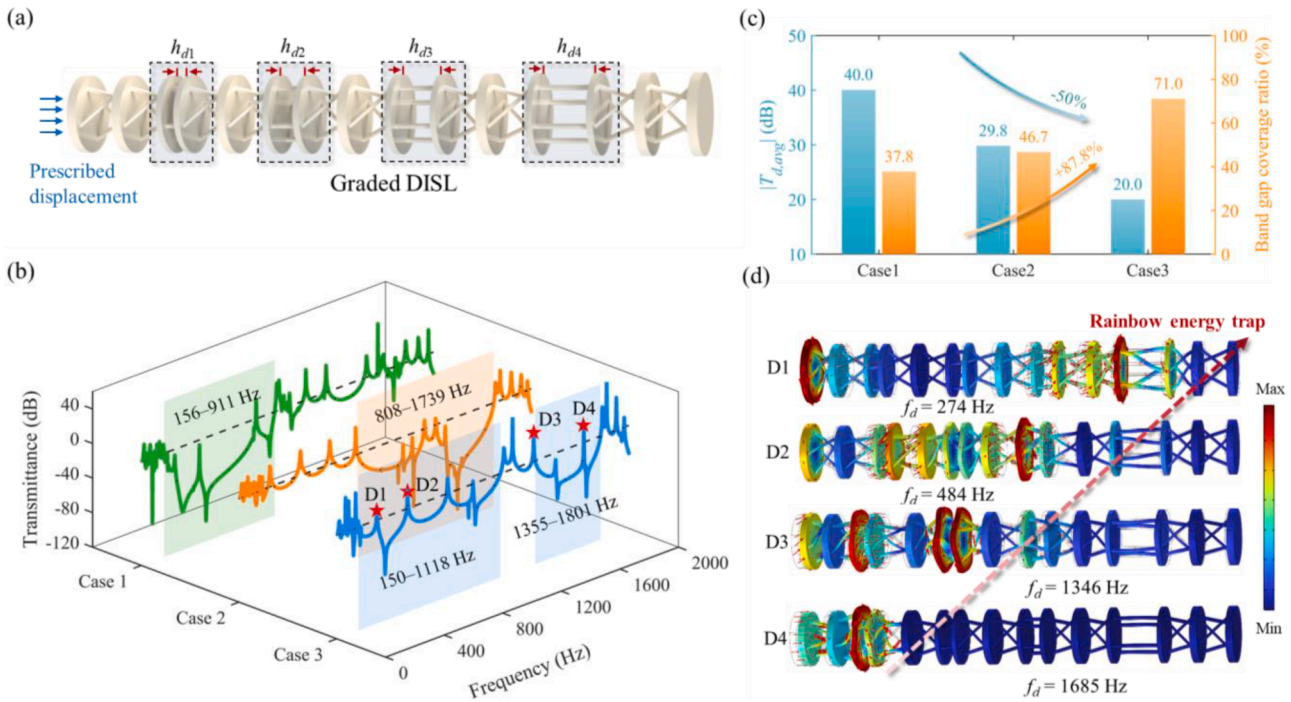

Fig. 8. (a) Schematic of the GDISL containing four defect units, where each has a distinct h_d; (b) Displacement transmittance for three GDISL configurations (Cases 1–3). The VLR band gap is highlighted by colored shading with the corresponding frequency range; (c) Variations of the average transmittance $T_{d,avg}$ and band gap coverage for Cases 1–3; (d) Mode shapes corresponding to defect-state peaks labeled by D1-D4 in (b).

3.3. Analysis of band gap tunability

In conventional LR metamaterials, band gap frequencies are primarily determined by the properties of the resonators. For example, in mass-spring-based metamaterials, the band gap boundaries depend on the resonator mass and stiffness [29,95]. By analogy, the frequency of the VLR band gap is expected to be governed by the torsional resonance characteristics of the defect. For the defect unit in the DISL shown in Fig. 5(a), we assume that the two discs undergo equal-amplitude torsional motion in opposite directions, i.e., $\varphi_{a1} = \varphi_a$, and $\varphi_{a2} = -\varphi_a$. Under the rigid-body assumption and for small rotation angles, the relative twist across the connecting elements is φ_{a1}-$\varphi_{a2} = 2\varphi_a$. The restoring torque acting on a single disc is therefore $\widetilde{\tau}_a(\varphi_{a1} - \varphi_{a2}) = 2\widetilde{\tau}_a\varphi_a$, where $\widetilde{\tau}_a$ is the equivalent torsional stiffness of the defect unit, as defined by Eq. (1). Accordingly, the torsional equation of motion for a single disc in the torsional resonance mode can be written as:

$$\widetilde{J}\ddot{\varphi}_a + C\dot{\varphi}_a + 2\widetilde{\tau}_a\varphi_a = T_e(t), \tag{14}$$

where $\widetilde{J} = \frac{1}{2}m_d(D_{md}/2)^2$ is the disc's polar moment of inertia, m_d and D_{md} are the mass and diameter of the disc in the defect unit, and $T_e(t)$ denotes the external torque applied to the disc. In the absence of external excitation and damping, the natural frequency of the torsional resonance mode is $\omega_t = \sqrt{2\widetilde{\tau}_a/\widetilde{J}}$. Therefore, the following analysis focuses on how variations in the defect unit's moment of inertia and torsional stiffness affect the VLR band gap.

Fig. 7(a) presents the displacement-transmittance heatmap for different D_{md} of the 12-unit DISL, while the other geometric and material parameters are the same as those used for the 12-unit DISL in SubSection 3.2. To highlight the VLR band gap region, the points where $T_d = 0$ dB are outlined by black contour lines, and both the band gap and defect-mode regions are marked. It is seen that the band gap shifts toward lower frequencies as D_{md} increases. This occurs because a larger D_{md} increases the moment of inertia $\widetilde{J}$, thereby reducing the natural frequency of the torsional resonance mode. The defect-state peak also moves to a lower frequency as D_{md} increases. Fig. 7(b) further displays the displacement-transmittance for D_{md} = 5.4 cm, 7.2 cm, and 9 cm, with colored shaded regions indicating the band gaps. To provide additional detail, Fig. 7(c) shows the variations of the band gap bandwidth and the average transmittance $T_{d,avg}$ within the gap as D_{md} changes, with the inset illustrating the appearance of the defect unit. With increasing D_{md}, the band gap gradually narrows, and the vibration-suppression strength weakens. This is because the larger $\widetilde{J}$ makes the defect unit more resistant to torsional motion, resulting in smaller angular acceleration under the same applied torque. In addition, Fig. 7(d) depicts the evolution of the displacement-transmittance heatmap as the disc height h_{md} varies. Fig. 7(e) shows the transmittance for h_{md} = 0.4 cm, 1.2 cm, and 2 cm. As evident from these figures, the band gap shifts toward lower frequencies as h_{md} increases. This is attributed to the higher disc mass associated with greater h_{md}, which increases the moment of inertia $\widetilde{J}$. Fig. 7(f) depicts the variation of the band gap bandwidth and the average transmittance $T_{d,avg}$ with changing h_{md}. Similar to the effect of increasing D_{md}, enlarging h_{md} leads to a narrower band gap and weaker vibration-suppression performance.

Secondly, we investigate how the defect unit's torsional stiffness $\widetilde{\tau}_a$ influences the VLR band gap. From Eq. (1), it follows that changes in the length l_d and diagonal spacing D_d of the defect unit's vertical rods modify the equivalent torsional stiffness. Note that $l_d = h_d$ and $D_d = \sqrt{2}\overline{D}_d$. Displacement-transmittance heatmaps are calculated for different values of h_d and $\overline{D}_d$, and the results are shown in Fig. 7(g) and (j). Fig. 7(g) shows that increasing h_d shifts the band gap to lower frequencies. This occurs because a larger h_d reduces the equivalent torsional stiffness, thereby lowering the torsional resonance frequency of the defect unit. Fig. 7(h) provides transmittance profiles for h_d = 2 cm, 3.5 cm, and 5 cm, with the VLR band gap shaded to clearly illustrate the frequency evolution. Fig. 7(i) displays the variation in band gap width and average transmittance $T_{d,avg}$ with h_d. It can be observed that as h_d increases, the band gap width gradually expands, while the average attenuation intensity initially increases and then becomes nearly constant when $h_d > 3$ cm. Fig. 7(j) shows that increasing $\overline{D}_d$ shifts both the

Table 2
Graded configurations and corresponding vibration attenuation ranges.

Cases	h_{d1} (cm)	h_{d2} (cm)	h_{d3} (cm)	h_{d4} (cm)	BG_1	BG_2
1	2.2	4.0	6.0	8.0	156-911Hz	/
2	1.4	1.5	1.6	1.7	808–1739Hz	/
3	1.2	1.4	2.0	5.0	150–1118Hz	1355–1801Hz

band gap and the defect-mode peak to higher frequencies. This behavior arises because a larger $\overline{D}_d$ increases the equivalent torsional stiffness of the defect unit, thereby raising the torsional mode frequency. This observation further supports that the band gap originates from a torsional resonance rather than from a translational resonance effect, since Eq. (1) indicates that the vertical rod's translational stiffness is insensitive to $\overline{D}_d$. Fig. 7(k) shows transmittance slices for $\overline{D}_d = 0.5$ cm, 2 cm, and 3.8 cm to illustrate the evolution of the band gap in more detail. Fig. 7(l) shows the corresponding variations in band gap width and average transmittance $T_{d,avg}$ with $\overline{D}_d$. It is evident that the band-gap width gradually decreases as $\overline{D}_d$ increases, while the average attenuation intensity first increases and then decreases, though the overall variation remains moderate. Overall, the effect of torsional stiffness on the band gap width is less pronounced than that of the rotational inertia.

3.4. Ultra-Wide band gap via graded design

In conventional LR metamaterials, the contribution of individual resonators to the band gap is relatively independent. This feature has led to the development of various non-uniform designs to optimize band-gap performance [96,97]. Among them, graded metamaterials are regarded as an effective approach for broadening vibration attenuation bands [98,99]. The core idea is to embed multiple resonators with distinct resonance frequencies, thereby arranging a series of band gaps across different frequency ranges to form a broadband quasi-band gap. Such a system typically generates multiple resonance peaks within the band gap, accompanied by a spatially selective energy distribution known as the rainbow effect [100]. To achieve continuous frequency coverage, adjacent discrete band gaps should be designed to overlap. In this section, a graded DISL (GDISL) is introduced to investigate the influence of discretely distributed virtual local resonators on vibration attenuation performance, thereby verifying the resonant nature of the VLR band gap.

The schematic of the GDISL is shown in Fig. 8(e). The chain consists of 14 units, among which units 3, 6, 9, and 12 use vertical rods to connect the discs, forming local defects. The remaining units adopt the ISL configuration, all with left-handed chirality. The four defect units are assigned different values of h_d (e.g., h_{d1}, h_{d2}, …, h_{d4}), to produce a gradual variation in equivalent torsional stiffness. Based on the parameter analysis in subSection 3.3, the disc thickness for the four defect units is set to $h_{md} = 0.5$ cm to obtain a smaller rotational inertia and thereby achieve a wider individual band gap. The remaining geometric and material parameters are consistent with those in the previous subsection. To ensure generality, three cases are considered and summarized in Table 2. Case 1 targets a broadened low-frequency band gap; Case 2 targets a broadened high-frequency band gap; and Case 3 aims to achieve an ultra-wide attenuation band. Notably, larger variations in h_d are used in Case 1, while smaller variations are applied in Case 2. This choice reflects the nonlinear dependence of band gap frequency on h_d (as shown in Fig. 7(g)): the band gap center shifts more rapidly with h_d at high frequencies. Therefore, careful selection of h_d is required to achieve an approximately uniform distribution of discrete band gaps in the graded configuration.

Fig. 8(a) presents the displacement transmittance results for the three cases. The corresponding vibration attenuation ranges are listed in Table 2, with the discrete attenuation regions labeled BG_1 and BG_2. In Case 1, the VLR band gap is shaded in green and spans 156–911 Hz. In Case 2, the vibration-suppression region, highlighted in orange, shifts to a higher frequency range. Both cases demonstrate a clear expansion of the effective bandwidth. Case 3 shows ultra-wide attenuation from 150 Hz to 1801 Hz. It is noted that under the graded configuration, the discrete suppression regions become more numerous, while their attenuation strength decreases. This occurs because, to achieve broader frequency coverage, the individual attenuation gaps cannot fully overlap. Continuous coverage, therefore, requires finer tuning of defect parameters.

To quantify this effect, Fig. 8(c) presents the average transmittance $|T_{d,avg}|$ within the vibration suppression region and the band gap coverage ratio over 0–2000 Hz for Cases 1–3. Cases 1 and 2 exhibit comparable band-gap coverage (37.8 % and 46.7 %, respectively). However, Case 2 shows a significantly weaker average attenuation level due to its shorter h_d, which results in a lower vibration intensity, as also indicated in Fig. 7(i). Case 3 achieves the largest band gap coverage ratio (71 %), yet it has the weakest average vibration intensity. Compared with Case 1, the band gap coverage of Case 3 over 0–2000 Hz increases by 87.8 %, whereas the average transmittance decreases by 50 %. Moreover, multiple defect-state peaks appear inside the band gap. Taking Case 3 as an example, its defect-state peaks are marked with red pentagrams, and their modal shapes are shown in Fig. 8(d). These modes exhibit spatial localization of vibration energy at 274 Hz, 484 Hz, 1346 Hz, and 1685 Hz, concentrating respectively on defect units 4 through 1, thereby demonstrating the rainbow energy-trapping effect. Overall, the GDISL demonstrates that the global vibration attenuation performance can be effectively optimized by introducing discrete virtual local resonators with different resonance frequencies, highlighting its flexible tunability and its potential to achieve ultra-wide vibration attenuation ranges.

In summary, the analyses in subSections 3.2–3.4 indicate that the VLR band gap is intrinsically associated with a local resonance mechanism. The band gap boundaries, bandwidth, and attenuation strength can be tuned by carefully adjusting the virtual local resonators' rotational inertia and torsional stiffness. Similar to conventional LR band gaps, this mechanism is independent of the lattice constant, enabling the flexible realization of wide sub-kilohertz band gaps in compact structures. Importantly, the VLR band gap offers two key advantages over traditional LR band gaps. First, traditional LR band gaps require a periodic array of physical resonators, which introduces considerable added mass and manufacturing complexity [87]. In contrast, the VLR band gap achieves strong wave attenuation through mode transition without the need to incorporate physical resonators. Second, although traditional LR band gaps generally provide stronger vibration suppression than Bragg scattering band (characterized by sharp anti-resonance dips in the transmittance), their bandwidths are typically narrow. Broadening such gaps commonly requires increasing the number or mass of the resonators [29], which inevitably raises structural weight. By comparison, the VLR band gap can be generated using only one or two virtual local resonators while still delivering a comparatively wide band with strong attenuation. Meanwhile, the band gap width and attenuation strength can be further increased by reducing the defect unit's rotational inertia (e.g., by decreasing the disc diameter), thereby improving performance while lowering the added mass.

4. Experimental validation

In this section, the proposed chirial metamaterial is fabricated and experimentally characterized. The experimental results are compared with numerical simulations to validate the low-frequency, broadband vibration attenuation performance and the tunability of the VLR band gaps.

Four prototypes are investigated. Prototype 1 consists of 12 unit cells with two defect units, identical to the DISL shown in Fig. 5(a). Prototype 2–4 comprises 14 unit cells with four graded defect units, corresponding

Table 3
Geometric properties of the metamaterial lattice (in cm).

D_m	h_m	$\overline{D}$	d	h	D_{md}	h_{md}	$\overline{D}_d$	h_d
6	0.8	3	0.36	2.5	6	0.5	3	4

to the GDISL configuration shown in Fig. 8(a). The geometric parameters of all prototypes are summarized in Table 3. Notably, in Prototype 2–4, the spacings between adjacent discs in the defect units (h_{d1}, h_{d2}, h_{d3}, h_{d4}) vary progressively, with values of (2,2.6, 4, 5) cm, (1.4, 1.5, 1.6, 1.7) cm, and (1.4, 1.6, 2, 5) cm, respectively. The specimens are fabricated using Esun PLA via 3D printing ($E = 3.2$ GPa, $\rho = 1000$ kg/m^3,$\nu = 0.41$). The experimental setup is depicted in Fig. 9(a). Each specimen is suspended by thin nylon strings to approximate free-free boundary conditions and

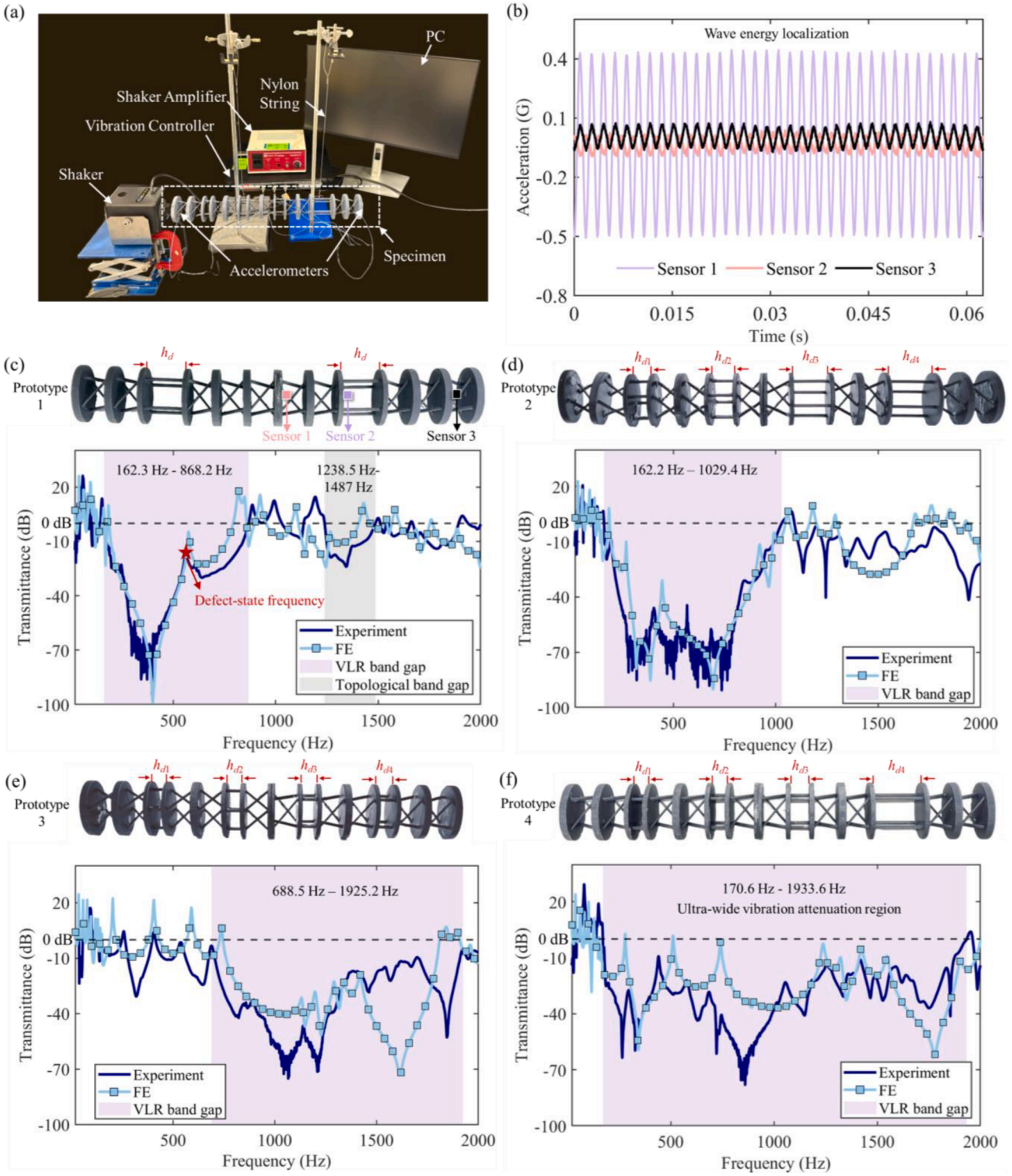

Fig. 9. (a) Experimental setup; (b) Measured acceleration amplitudes at the defect location (sensor 2) and non-defect locations (sensors 1 and 3) under harmonic excitation at the defect peak frequency ($f_d = 560.8$ Hz) for prototype 1. The sensor locations are indicated in (c); (c) Comparison between the numerical and experimental transmittance of prototype 1; (d-f) Comparison between the numerical and experimental transmittance of prototypes 2–4.

excited at the left end by an electrodynamic shaker to induce axial motion. Miniature ceramic accelerometers (PCB Piezotronics, model 352C23; mass: 0.2 g; sensitivity: 5.4 mV/g) are mounted at both ends to measure the transmittance. The experimental procedure is as follows. A frequency-swept harmonic excitation with acceleration amplitude of 0.5 g and a sweep rate of 100 Hz/minis generated by a vibration controller (Vibration Research, model VR9500), amplified by a power amplifier (SignalForce, model PA30E), and applied via an electrodynamic shaker (Labworks, model ET-132–2). Signal generation and response acquisition are performed using VibrationVIEW for post-processing.

Fig. 9(c) presents the measured transmittance of prototype 1, with the 0 dB reference indicated by a dashed line. A pronounced VLR band gap is observed in the frequency range of 162.3–868.2 Hz (shaded in pink), exhibiting a characteristic anti-resonance feature. In addition, a topological band gap appears in the range of 1238.5–1487 Hz (shaded in gray). For comparison, the corresponding FE-predicted transmittance is also plotted. To better approximate the behavior of a practical prototype, material damping is incorporated through a complex modulus formulation. The loss factor is set to $\zeta = 0.01$, and the Young's modulus of the metamaterial unit is expressed as $E\,(1 + \mathrm{i}\zeta)$. Fig. 9(c) shows that the experimental result agrees well with the numerical predictions, particularly within the band gap regions, where excellent correspondence is achieved. Some discrepancies appear at higher frequencies, where the modal peaks do not perfectly coincide. These deviations are expected, as the experimental setup cannot strictly reproduce ideal free-free boundary conditions, and the self-weight of the DISL specimen introduces additional effects. Notably, a distinct resonance peak is experimentally identified at 560.8 Hz within the VLR band gap, as marked by a pentagram. This peak is attributed to a defect state, as discussed in Section 3. To further examine this mode, a harmonic excitation at 560.8 Hz with an amplitude of 0.5 g is applied to the left end of prototype 1. Three sensors are used to record the time-domain responses: one located at the defect unit (Sensor 2) and two at the non-defect units (Sensors 1 and 3), as shown in Fig. 9(b). The results in Fig. 9(b) show that the vibration amplitude at the defect unit is significantly higher than that at the non-defect units, confirming the wave energy localization induced by the defect state.

Fig. 9(d)-(F) compares the experimental results of prototypes 2–4 with the FE predictions, showing good agreement in the overall band-gap trends. Owing to the graded design of the defect units, multiple discrete VLR band gaps are formed, effectively broadening the vibration attenuation range of the GDISL. In particular, for prototype 4, the relatively large spacing between the discrete VLR band gaps collectively results in an ultra-wide attenuation band spanning 170.6–1933.6 Hz. This demonstrates the strong potential of VLR band gaps for achieving superior vibration suppression over a broad frequency range using lightweight structures.

5. Conclusions

This work tackles the challenge of reconciling broadband low-frequency vibration suppression while maintaining lightweight and high-stiffness metamaterial designs. We proposed a novel defective isotatic lattice metamaterial incorporating a chiral-removed defect, which gives rise to a virtual locally resonant (VLR) band gap fundamentally distinct from conventional LR band gaps. Band structure and transmittance analysis reveal that the chiral-removed defect induces a mode transition in the compression-torsion coupled system, leading to the formation of a virtual torsional localized resonator responsible for opening the VLR band gap. The resonant mechanism and the flexible tunability of its low-frequency and broadband characteristics are systematically investigated through equivalent resonant-parameter analysis and graded unit design. Multiple prototypes with both uniform and graded configurations are fabricated, and transmission experiments validate the VLR concept.

Several key conclusions can be drawn. First, only defects that introduce an abrupt change in chirality can trigger the mode transition required to open a VLR band gap. Generic defects are insufficient. Second, unlike conventional LR mechanisms that require arrays of physical resonators, the VLR band gap can be generated by one or two virtual local resonators emerging at the defect. This mechanism enables a wide and strong band gap while alleviating the trade-off between lightweight design and broadband performance. Third, the onset frequency and bandwidth of the VLR band gap can be flexibly tuned by the rotational inertia and torsional stiffness of the defect unit. In particular, reducing the rotational inertia can broaden the band gap without incurring additional mass penalties. Fourth, because the VLR mechanism relies on an individual virtual torsional resonator, graded defect designs can produce overlapping broadband pseudo-gaps. Experimental results demonstrate that an ultra-broad low-frequency attenuation band spanning 170.6–1933.6 Hz can be achieved using only four graded defects.

In summary, this study demonstrates a chiral metamaterial featuring a novel VLR band gap mechanism, providing a new and efficient pathway for broadband low-frequency vibration suppression in lightweight structures.

Data availability statement

The data that supports the findings of this study are available within the article.

Declaration of competing interest

The authors declare that they have no known competing financial interests or personal relationships that could have appeared to influence the work reported in this paper.

Acknowledgments

Yupei Jian would like to gratefully acknowledge the National Natural Science Foundation of China (Grant Nos. 52505130, 52305135), Sichuan Science and Technology Program (Grant No. 2025ZNSFSC1268), and the China Postdoctoral Science Foundation (Grant No. 2024M762677).

References

[1] Hu S, Hao H, Meng D, Yang M. Theoretical and numerical study of the thermo-mechanical coupling effect on the fluid viscous damper. J Sound Vib 2025;597:118846.
[2] Rathod A, Vyavhare R. Retracted article: commercial truck ride comfort study: a literature review. Int J Dyn Control 2025;13:50.
[3] Isacchi G, Ripamonti F. A robust and fail-safe semi-active vertical damper to improve ride comfort. Veh Syst Dyn 2025;63:2039–61.
[4] Liu X, Chen S, Wang B, Tan X, Cao B, Yu L. A mechanical metamaterial with real-time tunable bandgap based on pneumatic actuation. Int J Mech Sci 2025;289:110045.
[5] Li L, Yang F, Liu S, Guo Z, Han D, Xia Y, et al. Design of quasi-zero-stiffness metamaterials with ultra-wideband vibration isolation performance. Int J Mech Sci 2025:110440.
[6] Li L, Wu J, Yang F, Li P, Lu G, Fan H, et al. Mechanisms of low-frequency bandgap formation and energy absorption of three-dimensional nested hybrid lattice structures. Compos B: Eng 2025;291:112045.
[7] Jian Y, Hu G, Tang L, Shen Y, Zhan Y, Aw K. Adaptive piezoelectric metamaterial beam: autonomous attenuation zone adjustment in complex vibration environments. Smart Mater Struct 2023;32:105023.
[8] Huang J, Wu S, Lin J, He D. Experimental study on load bearing and vibration suppression performance of beam-type metastructures. Eng Struct 2026;351:121999.
[9] Zhang X, Geng M, Zhao C, Cao Y, Wang P. Multi-gradient acoustic black hole metamaterial for near-perfect sound attenuation: theory, simulation and experiments. Appl Acoust 2025;231:110546.
[10] Lee D, Youn BD, Jo S-H. Deep-learning-based framework for inverse design of a defective phononic crystal for narrowband filtering. Int J Mech Sci 2023;255:108474.
[11] Zhang S, Wan Y, Bian X, Dong X. Broadband and controllable topological interface state of longitudinal wave in pillared phononic crystal beams. Phys B: Condens Matter 2023;650:414555.

[12] Jian Y, Tang L, Huang D, Han H, Liu W, Hu G. Designing an electromechanical metamaterial beam with arbitrary decoupled defect modes for multi-band wave localization. Smart Mater Struct 2025;34:035015.
[13] Roshdy M, Chen T, Nakhmanson S, Bilal OR. Tunable ferroelectric auxetic metamaterials for guiding elastic waves in three-dimensions. Extreme Mech Lett 2023;59:101966.
[14] Yuan W, Zhang Y, Pan Y, Huang Y, Zhao J, Yang F, et al. Topological rainbow trapping, concentration and guiding in graded elastic valley phononic crystal plate. Eng struct 2024;304:117596.
[15] Wang L, Chen Z, Cheng L. A metamaterial plate with magnetorheological elastomers and gradient resonators for tuneable, low-frequency and broadband flexural wave manipulation. Thin-Walled Struct 2023;184:110521.
[16] Cenedese M, Belloni E, Braghin F. Interaction of Bragg scattering bandgaps and local resonators in mono-coupled periodic structures. J Appl Phys 2021;129:124501.
[17] Jia Q, Han D, Wang C, Wen J, Yu D. Anisotropic-isotropic hybrid metamaterials for low-frequency wave attenuation. Int J Mech Sci 2025:110823.
[18] Deng J, Gao N, Chen X, Han B, Ji H. Evanescent waves in a metabeam attached with lossy acoustic black hole pillars. Mech Syst Signal Process 2023;191:110182.
[19] Hu B, Zhang Z, Yu D, Liu J, Zhu F. Broadband bandgap and shock vibration properties of acoustic metamaterial fluid-filled pipes. J Appl Phys 2020;128:205103.
[20] Vo NH, Pham TM, Bi K, Hao H. Model for analytical investigation on meta-lattice truss for low-frequency spatial wave manipulation. Wave Motion 2021;103:102735.
[21] Wang X, Xiong J. Integrated design of novel composite plate-truss hybrid lattice structures for superior energy absorption. Int J Solids Struct 2025:113447.
[22] Guo Z, Wen J, Yu D, Hu G, Yang Y. Widening the band gaps of hourglass lattice truss core sandwich structures for broadband vibration suppression. J Vib Acoust 2023;145:061002.
[23] Li H, Hu Y, Huang H, Chen J, Zhao M, Li B. Broadband low-frequency vibration attenuation in 3D printed composite meta-lattice sandwich structures. Compos B: Eng 2021;215:108772.
[24] An X, Sun G, Yuan X, Tian Y, Hou X, Fan H. Design of Kagome lattice composite sandwich metastructures with high load bearing and low frequency vibration reduction properties. Compos A: Appl Sci Manuf 2023;174:107716.
[25] Gao M, Tian X, Guo S, Zhong H, Jiang N. Embedded multi-resonator Honeycomb metamaterials for low-frequency broadband bandgaps. Thin-Walled Struct 2025:114292.
[26] Sun X-W, Tan M-T, Xu G-G, Cao Y, Wen X-D, Liu Z-J. Sub-wavelength topological boundary states and rainbow trapping of local-resonance phononic crystal plate. J Phys D Appl Phys 2024;57:225302.
[27] Lin Q, Zhou J, Wang K, Xu D, Wen G, Wang Q, et al. Low-frequency locally resonant band gap of the two-dimensional quasi-zero-stiffness metamaterials. Int J Mech Sci 2022;222:107230.
[28] Lei L, Miao L, Zheng H, Wu P, Lu M. Band gap extending of locally resonant phononic crystal with outward hierarchical structure. Appl Phys A 2022;128:492.
[29] Jian Y, Hu G, Tang L, Xu J, Aw KC. A generic theoretical approach for estimating bandgap bounds of metamaterial beams. J Appl Phys 2021;130:054501.
[30] Wang G, Wan S, Hong J, Liu S, Li X. Enhancement of the vibration attenuation characteristics in local resonance metamaterial beams: theory and experiment. Mech Syst Signal Process 2023;188:110036.
[31] Wang J, Bennett GJ. Incorporating extended neck Helmholtz resonators into an advanced multi-degree of freedom acoustic metamaterial for low-frequency, broadband acoustic absorption. Appl Acoust 2025;238:110750.
[32] Gautam A, Celik A, Azarpeyvand M. On the acoustic performance of double degree of freedom helmholtz resonator based acoustic liners. Appl Acoust 2022;191:108661.
[33] Wang X, Pang Y, Wu JH, Ma F. A broadband metamaterial damper design based on synergetic coupling among multi-cells. Appl Acoust 2023;206:109303.
[34] Jian Y, Tang L, Hu G, Li Z, Aw KC. Design of graded piezoelectric metamaterial beam with spatial variation of electrodes. Int J Mech Sci 2022;218:107068.
[35] Li X, Ma D, Xu X, Wang H, Jin F, Cheng J, et al. Graded dielectric metamaterial with designable permittivity fabricated by 3D printing. Adv Funct Mater 2025:e14533.
[36] Wang X, Xu Z-D, Dai J, Peng H, Chen Z, Wang Z, et al. Flutter behavior of functionally graded graphene origami-reinforced auxetic metamaterial composite laminated plates in supersonic flow. Eng Struct 2025;336:120318.
[37] Gomes C, dos Santos M, Araújo B, Pereira F, Nobrega E, Dos Santos J, et al. Wave and vibration attenuation in graded elastic metamaterial beams with local resonators. Int J Mech Sci 2025;293:110125.
[38] Fang X, Lacarbonara W, Cheng L. Advances in nonlinear acoustic/elastic metamaterials and metastructures. Nonlinear Dyn 2025;113:23787–814.
[39] Lou J, Zhang S, Fan H, Fang X, Du J. Ultra-low frequency and broadband flexural wave attenuation using an inertant nonlinear metamaterial beam. Eng Struct 2025;323:119169.
[40] Maurizi M, Xu D, Wang Y-T, Yao D, Hahn D, Oudich M, et al. Designing metamaterials with programmable nonlinear responses and geometric constraints in graph space. Nat Mach Intell 2025;7:1023–36.
[41] Wang T, Touzé C, Li H. Ding Q. Nonlinear dispersion relationships and dissipative properties of damped metamaterials embedding bistable attachments. Nonlinear Dyn 2025;113:30701–30.
[42] Huang Z, Wu J, Wang C, Yang S, Ma F. Resonant-scattering hybrid device for multiband acoustic topology valley transmission. Phys Rev B 2021;104:094110.
[43] Liang F, Chen Y, Kou H, Qian Y. Hybrid Bragg-locally resonant bandgap behaviors of a new class of motional two-dimensional meta-structure. Eur J Mech-A/Solids 2023;97:104832.
[44] Jin Y, Jia X-Y, Wu Q-Q, He X, Yu G-C, Wu L-Z, et al. Design of vibration isolators by using the Bragg scattering and local resonance band gaps in a layered honeycomb meta-structure. J Sound Vib 2022;521:116721.
[45] Zhang Z, Han X. A new hybrid phononic crystal in low frequencies. Phys Lett A 2016;380:3766–72.
[46] Frenzel T, Kadic M, Wegener M. Three-dimensional mechanical metamaterials with a twist. Science 2017;358:1072–4.
[47] Li H, Yao H, Li X, Xiao D, Shi C. Multi-frequency torsional vibration suppression of chiral metamaterial-rotor systems. Eng Struct 2025;342:120919.
[48] Li A, Bai Z-M, Yin X, Zhu T, Sun Z-Y, Yang J, et al. A tensegrity-inspired inertial amplification metastructure with tunable dynamic characteristics. J Mech Phys Solids 2025;196:106037.
[49] Ou H, Hu L, Wang Y, Liu C. High-efficient and reusable impact mitigation metamaterial based on compression-torsion coupling mechanism. J Mech Phys Solids 2024;186:105594.
[50] Zhang X, Liu Z, Lei J, Li S. Gradient metamaterials with tunable compression-twist coupling deformation. Acta Mech 2025;236:357–79.
[51] Wang S, Wang A, Wu Y, Li X, Sun Y, Zhang Z, et al. Ultra-wide band gap and wave attenuation mechanism of a novel star-shaped chiral metamaterial. Appl Math Mech 2024;45:1261–78.
[52] Ding W, Chen T, Yu D, Chen C, Zhang R, Zhu J, et al. Isotacticity in chiral phononic crystals for low-frequency bandgap. Int J Mech Sci 2024;261:108678.
[53] Chen M-R, Xu G-G, Song T, Liu X-X, Wen X-D, Sun X-W. Tunable ultrawide bandgaps in two-dimensional single-phase chiral meta-structures based on shape memory alloys. Mech Adv Mater Struct 2025:1–12.
[54] Yang C, Yang K, Tian Y, Fu M, Hu L. Theoretical analysis on the stiffness of compression-torsion coupling metamaterials. Extreme Mech Lett 2021;46:101336.
[55] Zhang X, Liu Z, Lei J, Li S. A novel 3D chiral metamaterial with overall compression-twist properties. Adv Eng Mater 2024;26:2401613.
[56] Yin C, Xiao Y, Zhu D, Wang J, Qin Q-H. Design of low-frequency 1D phononic crystals harnessing compression-twist coupling effect with large deflection angle. Thin-Walled Struct 2022;179:109600.
[57] Park J, Lee D, Jang Y, Lee A, Rho J. Chiral trabeated metabeam for low-frequency multimode wave mitigation via dual-bandgap mechanism. Commun Phys 2022;5:194.
[58] Wang K, Zhu J, Zhang R, Ding W, Liu H, Chen T. Magnetorheological intelligent chiral metamaterials with ultra-low frequency bandgap. Eng Struct 2026;351:122074.
[59] Zhao P, Zhang K, Hong F, Deng Z. Tacticity-based one-dimensional chiral equilateral lattice for tailored wave propagation and design of elastic wave logic gate. J Sound Vib 2022;521:116671.
[60] Lin Y, Ou H, He J, Wen G, Liu J. A bio-inspired metamaterial for attenuating vibration with a compression-torsion coupling effect. Mech Adv Mater Struct 2025:1–9.
[61] Yu D, Wang G, Zhao Q, Ding W, Hu G, Hong J. Isotactic and syndiotactic chiral mechanical metamaterials with tunable band gaps. Mech Syst Signal Process 2025;230:112602.
[62] Yu D, Zhao Q, Wang G, Hu G, Xi H, Li B, et al. Periodic and aperiodic hierarchical chiral metamaterials for broadband vibration suppression. Mech Syst Signal Process 2026;243:113704.
[63] Cunin CE, Meacham RF, Lee ER, Roh H, Samal S, Li W, et al. Leveraging insulator's tacticity in semiconducting polymer blends. ACS Appl Mater Interfaces 2024;16:39717–27.
[64] Zhao P, Wang Z, Zhu X, Wang T, Zhang K. Effect of tacticity on the dynamic response of chiral mechanical metamaterials. Acta Mech Solida Sin 2024;37:979–88.
[65] Zhao P, Zhang K, Qi L, Deng Z. 3D chiral mechanical metamaterial for tailored band gap and manipulation of vibration isolation. Mech Syst Signal Process 2022;180:109430.
[66] Bergamini A, Miniaci M, Delpero T, Tallarico D, Van Damme B, Hannema G, et al. Tacticity in chiral phononic crystals. Nat Commun 2019;10:4525.
[67] Ding W, Chen T, Chen C, Chronopoulos D, Assouar B, Wen Y, et al. Description of bandgaps opening in chiral phononic crystals by analogy with Thomson scattering. New J Phys 2023;25:103001.
[68] Ding W, Chen T, Chen C, Chronopoulos D, Zhu J, Assouar B. Thomson scattering-induced bandgap in planar chiral phononic crystals. Mech Syst Signal Process 2023;186:109922.
[69] Ding W, Chen T, Chen C, Chronopoulos D, Zhu J. A three-dimensional twisted phononic crystal with omnidirectional bandgap based on inertial amplification by utilizing translation-rotation coupling. J Sound Vib 2022;541:117307.
[70] Zhang H, Li Y, Tang L, Yao S, Peng Y. Topological elastic wave transport and manipulation in three-dimensional metamaterials stacked with sandwich plates. Eur J Mech-A/Solids 2025;109:105486.
[71] Li Y, Zhang H. Theoretical analysis on topological interface states of 1D compression-torsion coupling metamaterial. Compos Struct 2023;305:116556.
[72] Zhang H, Tang L, Li Y, Aw K. Tacticity-based chiral topological metamaterials for longitudinal and torsional wave manipulation. Int J Mech Sci 2025;286:109922.
[73] Park J, Lee G, Kwon H, Kim M, Rho J. All-polarized elastic wave attenuation and harvesting via chiral mechanical metamaterials. Adv Funct Mater 2024;34:2403550.

[74] Jian Y, Wang K, Xia C, Huang D, Han H, Hu G. Higher-order defective metamaterial for multi-band low-frequency vibration localization. Int J Mech Sci 2025:110859.
[75] Xiao H, Tan T, Li T, Zhang L, Yuan C, Yan Z. Enhanced multi-band acoustic energy harvesting using double defect modes of Helmholtz resonant metamaterial. Smart Mater Struct 2023;32:105030.
[76] Chen Q, Zhu Y, Zhang K, Feng K. Broadband low-frequency acoustic energy harvesting amplified by sonic crystal metamaterial with double defects. J Vib Eng Technol 2024;12:469–80.
[77] Hyun J, Jung J, Park J, Choi W, Kim M. Simultaneous low-frequency vibration isolation and energy harvesting via attachable metamaterials. Nano Converg 2024;11:38.
[78] Cai T, Huang S, Guo H, Yuan T, Sun P, Liu N. Sound insulation performance of membrane-type acoustic metamaterial based on defect state structure. Phys Scr 2024;99:025967.
[79] Xu J, Zhu D, Guo Z, Li X, Liu Y, Li M, et al. Topological interface state formation mechanism of zero Poisson's ratio metamaterial and its application in vibration reduction. Thin-Walled Struct 2025:114240.
[80] Wang Y, Di M, Ding C, Dong Y, Zhai S, Luo C, et al. Controllable and multi-band acoustic metamaterial topological insulators. J Phys D Appl Phys 2025;58:115303.
[81] Liu T, Lei Z. Low-frequency bandgap and tension-compression to twist mode transition of a novel pull-rotation chiral structure. J Phys D Appl Phys 2025;58:225301.
[82] Narang P, Garcia CA, Felser C. The topology of electronic band structures. Nat Mater 2021;20:293–300.
[83] Zhang K, Zhang P, Wang W, Zhang L, Wang P, Zhu X. Generating defect modes in resonator-based metamaterial using piezoelectric wafers. Smart Mater Struct 2026;35:015011.
[84] Zhang Q-M, Yang L, Fan Y-X, Tao Z-Y. Localization of elastic surface waves based on defect modes in non-Bragg structures. Phys Scr 2024;99:115267.
[85] Jo S-H, Shin YC, Choi W, Yoon H, Youn BD, Kim M. Double defects-induced elastic wave coupling and energy localization in a phononic crystal. Nano Converg 2021;8:27.
[86] Zhang M, Hu C, Yin C, Qin Q-H, Wang J. Design of elastic metamaterials with ultra-wide low-frequency stopbands via quantitative local resonance analysis. Thin-Walled Struct 2021;165:107969.
[87] Chang I-L, Liang Z-X, Kao H-W, Chang S-H, Yang C-Y. The wave attenuation mechanism of the periodic local resonant metamaterial. J Sound Vib 2018;412:349–59.
[88] Dong Y, Yao H, Du J, Zhao J, Jiang J. Research on local resonance and Bragg scattering coexistence in phononic crystal. Mod Phys Lett B 2017;31:1750127.
[89] Zhu D, Z-k Guo. Topological edge states in concave hexagonal gyroscope phononic crystals. J Acoust Soc Am 2025;157:4307–18.
[90] Deinega A, Valuev I. Long-time behavior of PML absorbing boundaries for layered periodic structures. Comput Phys Commun 2011;182:149–51.
[91] Slobozhanyuk AP, Ginzburg P, Powell DA, Iorsh I, Shalin AS, Segovia P, et al. Purcell effect in hyperbolic metamaterial resonators. Phys Rev B 2015;92:195127.
[92] Zouari S, Brocail J, Génevaux J-M. Flexural wave band gaps in metamaterial plates: a numerical and experimental study from infinite to finite models. J Sound Vib 2018;435:246–63.
[93] Sugino C, Leadenham S, Ruzzene M, Erturk A. An investigation of electroelastic bandgap formation in locally resonant piezoelectric metastructures. Smart Mater Struct 2017;26:055029.
[94] Xiao Y, Wen J. Closed-form formulas for bandgap estimation and design of metastructures undergoing longitudinal or torsional vibration. J Sound Vib 2020;485:115578.
[95] Liu Z, Rumpler R, Feng L. Locally resonant metamaterial curved double wall to improve sound insulation at the ring frequency and mass-spring-mass resonance. Mech Syst Signal Process 2021;149:107179.
[96] Thomes RL, Mosquera-Sánchez JA, De Marqui Jr C. Bandgap widening by optimized disorder in one-dimensional locally resonant piezoelectric metamaterials. J Sound Vib 2021;512:116369.
[97] Qin X, Zhao P, Yang W, Wangechi V, Cheng N. Noise reduction performance of non-uniform resonant cavity periodic array noise barriers. Phys Scr 2026;101:055501.
[98] Jian Y, Hu G, Tang L, Xu J, Huang D, Aw K. Graded metamaterial with broadband active controllability for low-frequency vibration suppression. J Appl Phys 2024;136:043108.
[99] Yang F, Ma Z, Guo X. Bandgap characteristics analysis and graded design of a novel metamaterial for flexural wave suppression. Appl Math Mech 2025;46:1–24.
[100] Soliman SE, Barlou M, Tsakmakidis KL, Wong ZJ. Rainbow trapping for advanced wave control. Adv Phys: X 2025;10:2517551.